AGU ADVANCING EARTH AND SPACE SCIENCE

JGR Atmospheres

RESEARCH ARTICLE
10.1029/2022JD036648

GNSS Radio Occultation Infilling of the African Radiosonde Data Gaps Reveals Drivers of Tropopause Climate Variability

Tong Ding[1], Joseph L. Awange[1], Barbara Scherllin-Pirscher[2], Michael Kuhn[1], Khandu[3], Richard Anyah[4], Ayalsew Zerihun[5], and Luyen K. Bui[6,7]

[1]School of Earth and Planetary Sciences, Spatial Sciences Discipline, Curtin University, Perth, WA, Australia, [2]Zentralanstalt für Meteorologie und Geodynamik, Vienna, Austria, [3]Landgate (formerly the Department of Land Information), Perth, WA, Australia, [4]Department of Natural Resources and the Environment, University of Connecticut, Storrs, CT, USA, [5]School of Molecular and Life Science, Curtin University, Perth, WA, Australia, [6]Department of Civil and Environmental Engineering, University of Houston, Houston, TX, USA, [7]Faculty of Geomatics and Land Administration, Hanoi University of Mining and Geology, Hanoi, Vietnam

Abstract Radiosonde data are important for understanding and monitoring the upper troposphere and lower stratosphere (UTLS) region. Over much of Africa, however, such data are lacking; consequently, the African UTLS is understudied, and potential proxies such as climate models and reanalysis products fail to fully capture the behavior of the UTLS. This study pioneers the use of Global Navigation Satellite System-Radio Occultation (GNSS-RO) data from 2001 to 2020 to address the radiosonde data gap over Africa and contributes to a better understanding of the tropopause (TP) characteristics under the influence of global and regional climate drivers over the continent. As a first step to using GNSS-RO for infilling the radiosonde data gap over Africa, we analyzed the performance of GNSS-RO (2001–2020) and reanalysis products (European Centre for Medium-Range Weather Forecasts Reanalysis 5 (ERA5) and Modern-Era Retrospective analysis for Research and Applications version 2 (MERRA-2)) against radiosonde observations applying the Kling-Gupta Efficiency metric. The analyses show that GNSS-RO data from Challenging Mini-satellite Payload, Gravity Recovery and Climate Experiment, Meteorological Operational, Constellation Observing System for Meteorology, Ionosphere, and Climate (COSMIC), and COSMIC-2 are in good agreement with radiosonde measurements with differences being smaller than 1 K in the UTLS, thereby enabling infilling of missing radiosonde data in Africa during 2001–2020. By contrast, the smoothed vertical temperature profiles of reanalysis products lead to a warm bias of +0.8 K in ERA5 and +1.2 K in MERRA-2 and these biases alter some vertical and temporal structure details, with possible implications on climate change detection and attribution. Furthermore, the analysis of GNSS-RO data over Africa revealed: (a) the teleconnections of El Niño-Southern Oscillation (ENSO), Quasi-Biennial Oscillation (QBO), Indian Ocean Dipole (IOD), Madden-Julian Oscillation (MJO), North Atlantic Oscillation (NAO) and Southern Annular Mode (SAM) at the tropopause boundary; (b) multiple coupled global climate drivers such as ENSO-IOD, ENSO-MJO, ENSO-NAO, QBO-IOD, and ENSO-NAO-MJO; (c) coupled global and regional climate drivers that influence the TP variability, for example, ENSO-Inter Tropical Convergence Zone; and (d), the deep convection associated with the Asian Summer Monsoon and Tropical/African Easterly Jet also locally influence TP height. In conclusion, this study demonstrates the capability of GNSS-RO to fill the vast radiosonde data gap over Africa. This opens the opportunity for further detailed studies toward a better understanding of the tropopause characteristics including localization, quantification of trends, and influences of global, regional, and coupled climate drivers.

Key Points:

- Global Navigation Satellite System-Radio Occultation (GNSS-RO) is capable of infilling the vast radiosonde data gap over Africa
- GNSS-RO captures global and regional climate drivers of tropopause behavior
- GNSS-RO reveals multiple coupled global and regional climate drivers

Supporting Information:

Supporting Information may be found in the online version of this article.

Correspondence to:

T. Ding,
tong.ding@student.curtin.edu.au

Citation:

Ding, T., Awange, J. L., Scherllin-Pirscher, B., Kuhn, M., Khandu, Anyah, R., et al. (2022). GNSS radio occultation infilling of the African radiosonde data gaps reveals drivers of tropopause climate variability. *Journal of Geophysical Research: Atmospheres*, *127*, e2022JD036648. https://doi.org/10.1029/2022JD036648

Received 16 FEB 2022
Accepted 11 AUG 2022

Author Contributions:

Conceptualization: Joseph L. Awange
Data curation: Tong Ding
Formal analysis: Tong Ding, Barbara Scherllin-Pirscher, Richard Anyah
Investigation: Tong Ding
Methodology: Tong Ding, Joseph L. Awange, Barbara Scherllin-Pirscher, Michael Kuhn
Resources: Joseph L. Awange, Barbara Scherllin-Pirscher, Michael Kuhn, Khandu, Ayalsew Zerihun
Software: Tong Ding
Validation: Khandu
Visualization: Tong Ding, Joseph L. Awange, Luyen K. Bui
Writing – original draft: Tong Ding

1. Introduction

In Africa, which has high vulnerability to impacts of extreme weather events and climate change (IPCC, 2014), there is paucity of surface- and upper-air observations. The alarming state of the issue has been highlighted recently by the World Meteorological Organization (WMO, 2020), which states that "there is a dramatic decrease of almost 50% from 2015 to 2020 in the number of radiosonde flights and/or observations, the most important type of surface-based observations for weather prediction and climate analysis" and furthermore, "now has poorer geographical coverage." Over the last two decades, some 82% of the countries in Africa have experienced severe (57%) and moderate (25%) radiosonde data gap. For Africa, in particular, where many studies have indicated a possible increase in the frequency and severity of climate extremes (droughts and floods) (Agutu et al., 2017; Awange, 2021a, 2021b), increased water stress (Terink et al., 2013), and food security risks (Awange, 2022;

Writing – review & editing: Tong Ding, Joseph L. Awange, Barbara Scherllin-Pirscher, Michael Kuhn, Khandu, Richard Anyah, Ayalsew Zerihun, Luyen K. Bui

Gregory et al., 2005), the situation is dire, prompting a call by Peuch (2020) for urgent need to fill the data gap in Africa and globally.

Radiosondes from weather balloons have conventionally been used as means of measuring atmospheric profiles of humidity, temperature, pressure, wind speed and direction. High quality, spatially and temporally "continuous" data from upper-air monitoring along with surface observations are critical bases for understanding weather conditions and climate trends, and providing weather and climate information for the welfare of societies. Reliable and timely information underpin society's preparedness to extreme weather conditions, and to changing climate patterns. Africa, however, suffers from insufficient, non-consistent in situ data, and poor data quality (Thomson et al., 2011). Moreover, the weather balloons rely heavily on the amount of gas fuel used and are usually launched at specific time intervals (e.g., every 6–12 hr) from airports or other approved locations. Additionally, the commonly used hydrogen generator is an expensive instrument that requires consistent maintenance and technical expertise, which is out of reach for most African countries. Other challenges pertaining to the African radiosonde data include systematic error in data and misaligned time series (see, e.g., Ramella-Pralungo et al., 2014; Wang & Zhang, 2008). These have led to the requirement of a re-evaluation of African radiosonde observation reliability (Lanzante et al., 2003; van der Linden et al., 2020).

Despite the establishment of the African monsoon multidisciplinary analysis (AMMA) radiosonde program to address data quality of radiosonde stations over West Africa, 30% of the data are still lost due to persistent technical failures (Fink et al., 2011). Moreover, Thorne and Vose (2010) reported heterogeneity of the in situ radiosonde record and its potential impact on long-term reanalyses, particularly over Africa (Lanzante et al., 2003; van der Linden et al., 2020). Further issues include temporal and spatial difficulties for long-term modeling (Seidel et al., 2004), limited data coverage in the Southern Hemisphere (SH) (Awange, 2018), challenges of operating over the ocean (Awange, 2012), and high operational costs (Parker et al., 2008). With vast data gaps in such a large part of the global landmass, home to some of the most vulnerable societies, the aforementioned call has galvanized a global effort (Taalas et al., 2021) to "plug the data gaps" in the decade ahead and halt a further deterioration in the observation networks.

The use of global reanalysis products could alleviate these challenges. However, different reanalysis products exhibit considerable discrepancies in regional studies (Chen et al., 2014). Additionally, differences in the responses of global temperature to volcanic eruptions (Fujiwara et al., 2015) and biases associated with the reanalyses of low vertical resolution (Meng et al., 2021) lead to different upper troposphere and lower stratosphere (UTLS) structures among reanalysis products and therefore to different tropopause characteristics (Homeyer et al., 2010). Recently, the fifth-generation reanalysis (ERA5) of the European Centre for Medium-Range Weather Forecasts (ECMWF) has been added to the plethora of tropopause monitoring products offering higher vertical resolution than previous reanalysis data sets. However, its performance against in situ observations over Africa's upper-air region has not been investigated yet.

In light of these shortcomings over Africa, Isioye et al. (2015) proposed the exploration of space-based techniques such as Global Navigation Satellite System (GNSS)-Radio Occultation (GNSS-RO) for addressing the radiosonde data gaps. The inception of the GNSS-RO technique that utilizes GNSS signals onboard of Low Earth Orbit (LEO) satellites to remotely sense the Earth's atmosphere has emerged as a state-of-the-art data set over the last two decades, providing high vertical resolution atmospheric temperature profiles around the tropopause region (see, e.g., Scherllin-Pirscher et al., 2021, and the references therein). Examples include the Challenging Mini-satellite Payload (CHAMP), the Gravity Recovery and Climate Experiment (GRACE), GRACE Follow-On (GRACE-FO), the Meteorological Operational (MetOp) satellites, and the Constellation Observing System for Meteorology, Ionosphere, and Climate (COSMIC). They have operated continuously around the globe under all-weather conditions, and offer millions of consistent measurements (Angerer et al., 2017) that are successfully assimilated into global reanalyses to improve global weather predictions and climate modeling (Ho et al., 2020). Awange (2012, 2018) showed that GNSS-RO can improve the deficiency of high-quality data in remote areas, which cannot be achieved by radiosondes alone. The recently launched COSMIC-2 mission (Anthes & Schreiner, 2019; Schreiner et al., 2020) increased sampling density at low- and mid-latitudes and provides reams of near-real-time data for weather research (Lien et al., 2021). The innovation of COSMIC-2 has enormously extended the data coverage and thereby significantly filled the data gaps over Africa. Nevertheless, the COSMIC-2 products have neither been tested nor explored over the African continent yet.

Clearly, infilling of the African continent's UTLS will benefit the understanding of its climate, which is influenced by numerous global, regional, and local climate variability modes, for example, the Indian Ocean Dipole (IOD; Saji et al., 1999), El Niño-Southern Oscillation (ENSO; Scherllin-Pirscher et al., 2012), North Atlantic Oscillation (NAO; Hurrell et al., 2003), Southern Annular Mode (SAM; Fogt et al., 2011), Madden-Julian Oscillation (MJO; Wheeler & Hendon, 2004), Quasi-Biennial Oscillation (QBO; Baldwin et al., 2001), the Inter Tropical Convergence Zone (ITCZ; Basha et al., 2015), the Tropical Easterly Jet (TEJ; Nicholson & Klotter, 2021), West African Monsoon (WAM; Sultan & Janicot, 2003), growing ozone pollution in Southern Africa (Thompson et al., 2014), and changing climate in the mountainous region (Kubokawa et al., 2016). Even though these climate drivers are known to trigger multi-effect severe weather and climate conditions (e.g., Awange, 2022; Awange et al., 2013), there are only a few studies that attempt to understand the African tropopause variability in relation to these climate drivers.

Indeed, that the tropopause, a boundary (i.e., 9–17 km) between the stratosphere and the troposphere could offer the possibility to quantitatively analyze upper level atmospheric characteristics in relation to regional climate variability and change over Africa is supported by regional studies that have been conducted, for example, in Australia (Khandu et al., 2011), Ganges-Brahmaputra-Meghna basin (Khandu et al., 2016), South America (Nascimento et al., 2020), and the tropical and subtropical tropopause regions (Tegtmeier et al., 2020). These studies were motivated by Santer, Sausen, et al. (2003) and Santer, Wehner, et al. (2003) who reported that the warming of the upper troposphere (UT, e.g., due to increased greenhouse gas emissions) and cooling of the lower stratosphere (LS, e.g., due to stratospheric ozone depletion) lead to a rise in tropopause height, indicating that climate change impacts can be quantified through UTLS monitoring. Subsequently, many studies on monitoring the global tropopause have explored various data sets ranging from in situ radiosonde to high vertical resolution data acquired from LEO satellites, that is, satellite-based data (e.g., Shangguan et al., 2019), radiosonde data (e.g., Feng et al., 2012), and reanalysis products (e.g., Xian & Homeyer, 2019). Nonetheless, such global tropopause assessments have limited physical implications and spatial importance at regional scales such as Africa (Franzke et al., 2020). For example, recent studies on global tropopause by Xian and Homeyer (2019) and tropical tropopause characterization by Tegtmeier et al. (2020) revealed large spatial inconsistencies between reanalyses and observations over equatorial Africa. A comprehensive and in-depth analysis of tropopause characteristics over Africa is, thus, still missing.

Despite almost two decades of advancement in the application of GNSS-RO globally and regionally, its use in Africa's climate-related studies has not been explored. This study, therefore, takes advantage of the 20 years (2001–2020) of GNSS-RO data over Africa from multiple missions to (a) statistically compare and validate GNSS-RO (including the latest COSMIC-2) profiles against radiosonde and reanalysis products (including the state-of-the-art ERA5), (b) address the missing radiosonde data and assess reanalysis products of Modern-Era Retrospective analysis for Research and Applications version 2 (MERRA-2) and ERA5, and finally (c), use the GNSS-RO and reanalysis products to assess the tropopause variability over Africa in relation to global (e.g., ENSO, IOD, NAO, SAM, MJO, and QBO), regional (e.g., ITCZ, TEJ, WAM, and regional ozone variability), and local climate drivers (e.g., impacts of local air-ocean interaction on tropopause).

2. Data and Methods

2.1. Data

2.1.1. Radiosonde

Radiosonde data used in this study are obtained from Integrated Global Radiosonde Archive version 2 (IGRA v2), an improvement of IGRA version 1 (Durre et al., 2016, 2018, https://www1.ncdc.noaa.gov/pub/data/igra/). The IGRA data provide primary atmospheric variables (i.e., geopotential height, temperature, relative humidity, pressure, and wind speed, etc.) at the mandatory, significant, tropopause, and surface pressure levels (Durre et al., 2006) for each launch time. WMO archives radiosonde station information across the globe and provides each radiosonde station's historical and operational status, including location, latitude, longitude, declared reporting status, type of station, WMO identifier, and elevation (World Meteorological Organization, 2020, https://www.wmo.int/datastat). In this study, WMO data are used to reevaluate the African radiosonde network. Problematic radiosonde data are identified if the radiosonde profile has less than five temperature readings. Furthermore, low-quality data are identified if the balloon did not reach the desired pressure level (i.e., at least 30–70 hPa

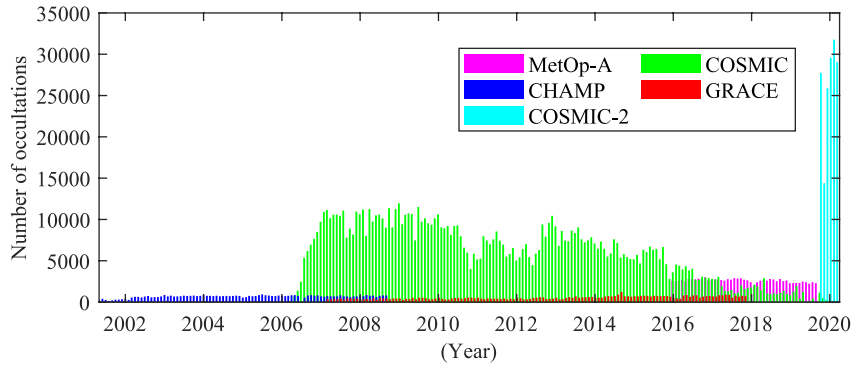

Figure 1. Temporal evolution of the number of Global Navigation Satellite System-Radio Occultation dry temperature profiles that were used to study tropopause variability and infill the radiosonde data gaps over Africa from May 2001 to April 2020. The figure shows the number of monthly observations provided by Challenging Mini-satellite Payload, Gravity Recovery and Climate Experiment, Constellation Observing System for Meteorology, Ionosphere, and Climate (COSMIC), Meteorological Operational satellite-A, and COSMIC-2.

dependent on the region). Neither problematic nor low-quality radiosonde data are used for comparison with GNSS-RO and reanalysis data in this study.

2.1.2. GNSS-RO

GNSS-RO measurements used in this study are provided by the COSMIC Data Analysis and Archive Center (CDAAC; https://cdaac-www.cosmic.ucar.edu/cdaac/doc/about.html). Multiple products, including raw measurements and retrieved atmospheric profiles are made available. CDAAC is a processing and service center for data collected from various RO missions such as Challenging Mini-satellite Payload (CHAMP; 2001–2008), Gravity Recovery and Climate Experiment (GRACE; 2007–2017), Constellation Observing System for Meteorology, Ionosphere, and Climate (COSMIC; 2006–2020), Meteorological Operational satellite–A (MetOp–A; 2016–2019), and Constellation Observing System for Meteorology, Ionosphere, and Climate–2 (COSMIC-2; 2019–2020). CHAMP, launched in July 2000 to succeed the first proof-of-concept occultation mission Global Positioning System/Meteorology (GPS/MET), collected approximately 650 vertical profiles over Africa per month, summing up to 59,620 profiles from May 2001 to October 2008 (see Figure 1). Note that CHAMP did not collect observations from 3 July 2006 to 8 August 2006 due to technical issues (Foelsche et al., 2008).

GRACE, a US/German collaborative mission, was launched in March 2002 and provided the first occultation observation on 28 July 2004 (Wickert et al., 2005). Before 2007, its data were not made available from CDAAC. It has provided approximately 530 profiles over Africa per month, with a total of 68,537 profiles from February 2007 to November 2017 (see Figure 1). The GRACE satellite mission ended in 2017 and was succeeded by the GRACE-FO mission launched on 22 May 2018, whose products were not available at CDAAC at the time of this study. The number of GNSS-RO profiles has grown considerably since the successful launch of the COSMIC constellation of six satellites in 2006 (see Figure 1). COSMIC is a joint project between the Taiwanese National Space Program Office (NSPO) and University Corporation for Atmospheric Research (UCAR). The constellation provided approximately 5,800 profiles over Africa per month, that is, a total of 991,691 vertical profiles between April 2006 and April 2020. Note that COSMIC exhibits data gaps of RO profiles between 1 April 2019 and 30 September 2019, due to decommissioning of the mission. Therefore, post-processed MetOp-A data are used, which provided approximately 2,600 profiles per month and a total of 117,043 profiles from January 2016 to September 2019.

Following the successful operation of the COSMIC mission, the next generation COSMIC-2/FORMOSAT-7 was launched on 25 June 2019, providing approximately 30,000 high-quality profiles over Africa per month. As shown in Figure 1, COSMIC-2 has an increased number of profiles over Africa due to the low inclination of the six COSMIC-2 satellites, which leads to a higher measurement density at low- and mid-latitudes (Schreiner et al., 2020) compared to other RO missions. Daily COSMIC-2 data are published by CDAAC at 02:00 UTC on the following day. The constellation has collected a total of 192,608 vertical atmospheric profiles over Africa from October 2019 to April 2020 (see Figure 1).

In this study, GNSS-RO profiles are excluded if the identified tropopause temperature and height exceed the range of 150–250 K and 5–25 km, respectively. Tropopause parameters are obtained from dry atmospheric products, which accurately describe "real" physical conditions in regions where humidity is low (see, e.g., Kursinski et al., 1997; Scherllin-Pirscher, Kirchengast, et al., 2011).

Previous studies examined the consistency of GNSS-RO data sets from different missions. Different COSMIC satellites were found consistent, with root mean square differences of fractional refractivity smaller than 0.2% between 10 and 20 km (Anthes et al., 2008; Schreiner et al., 2007). Ho et al. (2009) showed that the mean differences of CHAMP and COSMIC are within −0.35 K and +0.25 K, with the standard deviation increasing from 2 K in the mid-troposphere to 4 K at 10 hPa.

The sampling error primarily affects differences between GNSS-RO climatological fields from different missions. This error can be estimated and subtracted (Foelsche et al., 2009). Sampling error-corrected climatological fields of individual COSMIC satellites and CHAMP agree within 0.1 K between 8 and 30 km (see e.g., Foelsche et al., 2009, 2011; Steiner et al., 2011). In addition, Angerer et al. (2017) pointed out the fact that global temperature fields from GNSS-RO are highly consistent between 8 and 25 km, where differences from the multi-satellite average are smaller than 0.1 K for all satellites. Therefore, the data sets from the five GNSS-RO missions considered in this study are highly consistent within the 8–25 km region.

2.1.3. Reanalyses

The reanalysis data sets used in this study are temperatures, pressures, and geopotential heights provided by ECMWF Reanalysis 5 (ERA5) and Modern-Era Retrospective analysis for Research and Applications-version 2 (MERRA-2) for the period consistent with that of GNSS-RO data sets (May 2001–April 2020). ERA5 is the fifth generation ECMWF reanalysis (https://apps.ecmwf.int/data-catalogues/era5/?class=ea), replacing the ERA-Interim reanalysis (Hersbach et al., 2020). It provides hourly atmospheric profiles at 137 model pressure levels on a global 0.25° × 0.25° grid. ERA5 combines model data with observations from across the world through data assimilation to produce the best estimates of the state of the atmosphere, and has an improved spatial and temporal resolution compared to MERRA-2 (see Table 1(I)). Note that the ERA 5.1 is employed in this study for the period of 2001–2006 to avoid the tropopause cold bias (Simmons et al., 2020). ERA5 is used for the remaining period.

The MERRA-2 data have a spatial resolution of 0.5° × 0.625° and a consolidated vertical grid at 72 model levels (Gelaro et al., 2017, https://disc.gsfc.nasa.gov/datasets). Model level products of both ERA5 and MERRA-2 are used from 2001 to 2020 since they offer higher vertical resolution profiles.

2.1.4. Climate Variability Indices

The global climate variability indices used in this study are ENSO (Trenberth & Stepaniak, 2001), NAO (Hurrell et al., 2003), IOD (Saji et al., 1999), QBO (Baldwin et al., 2001), MJO (Wheeler & Hendon, 2004), and SAM (Marshall, 2003). All climate indices are obtained from May 2001 to April 2020. Table 1(II) provides a summary of the indices used. MJO, SAM, and NAO are smoothed with a 3-month moving average to reveal mid- and long-term variability, while provided ENSO, QBO, and IOD indices have already been smoothed. The smoothed indices are checked against the raw indices to avoid over-smoothing that can lead to loss of climate variability patterns (see, e.g., Hansen et al., 1998). No over-smoothed indices are detected.

Indices of regional climate drivers are calculated from zonal wind at 150 hPa (TEJ). Intertropical Convergence Zone (ITCZ) is represented by Outgoing Longwave Radiation (OLR; Basha et al., 2015) while the Western African Monsoon (WAM) is captured through rainfall data provided by Precipitation Estimation from Remotely Sensed Information using Artificial Neural Networks (PERSIANN; Hsu et al., 1997). PERSIANN contains the highest signal-to-noise ratio (SNR) and is thereby a suitable product to be employed over Africa (see, e.g., Awange et al., 2016). The southern Africa total ozone index is based on monthly area-averaged ozone values derived from an assimilation product that contains 15 different types of satellites observations. This type of ozone data has very few data gaps, but is only available from May 2001 to December 2018 (Copernicus Climate Change Service, 2018). Zonal wind and OLR are obtained from the NCEP reanalysis-1 (R1) provided by the National Oceanic and Atmospheric Administration (NOAA) Earth System Research Laboratories (ESRL; Kalnay et al., 1996). In this study, the NCEP reanalysis serves as an independent data source.

Table 1
Summary of Data Used in This Study

(I) Radiosonde, GNSS-RO and reanalysis products				
Source	Temporal resolution	Spatial resolution	Vertical resolution at UTLS (m)	Period
Radiosonde (IGRA V2)	6 hourly or 12 hourly	50 stations	N/A	May 2001–April 2020
CHAMP	650 profiles/month	Global	≈100–300 (Scherllin-Pirscher et al., 2021)	May 2001–October 2008
GRACE	530 profiles/month	Global		February 2007–November 2017
COSMIC	5,800 profiles/month	Global		April 2006–April 2020
COSMIC-2	30,000 profiles/month	45°S–45°N		October 2019–April 2020
MetOp-A	2,600 profiles/month	Global		January 2016–September 2019
ERA5	Hourly and monthly	0.25° × 0.25°	≈350 (Hersbach et al., 2020)	May 2001–April 2020
MERRA-2	3 hourly and monthly	0.5° × 0.625°	≈500 (Gelaro et al., 2017)	May 2001–April 2020

(II) Climate indices			
Climate driver	Region	Variables	Url
NAO	20°N–80°N; 90°W–40°E	Sea level pressure (SLP) anomaly	https://climatedataguide.ucar.edu/sites/default/files/nao_pc_monthly.txt
IOD	(i) 50°E–70°E; 10°S–10°N (ii) 90°E–110°E; 10°S–10°N	Sea surface temperature (SST) gradient	https://psl.noaa.gov/gcos_wgsp/Timeseries/DMI
ENSO	5°N–5°S; 170°W–120°W	SST anomaly (Niño 3.4)	https://psl.noaa.gov/data/correlation/nina34.data
QBO	10°N–10°S	Zonal-mean winds at 50 hPa	https://www.cpc.ncep.noaa.gov/data/indices/qbo.u50.index
SAM	40°S–65°S	Zonal-mean SLP	https://legacy.bas.ac.uk/met/gjma/sam.html
MJO	Equatorward of 30°N, 20°E	200-hPa velocity potential anomalies	https://www.cpc.ncep.noaa.gov/products/precip/CWlink/MJO/mjo.shtml
ITCZ	30°E–38°E; 13°N–18°N	OLR	https://psl.noaa.gov/data/timeseries/
TEJ	5°W–15°E; 5°N–15°N	Zonal-mean wind at 150 hPa	
Total ozone	10°E–35°E; 25°S–40°S	Area-averaged total ozone	doi:https://doi.org/10.24381/cds.4ebfe4eb
WAM	5°W–5°E; 6°N–8°N	Precipitation	http://chrsdata.eng.uci.edu/

2.2. Method

This study follows the workflow presented in Figure 2. First, GNSS-RO data are obtained from the various missions. Second, co-located (within 100 km and 3 hr) GNSS-RO profiles, radiosonde observations, and reanalysis products are identified to conduct a thorough statistical validation and comparison. Then, tropopause temperature and height are obtained from individual profiles and gridded into 2° × 2° monthly climatological fields. The sampling error is estimated and subtracted from monthly mean GNSS-RO fields (Foelsche et al., 2011; Scherllin-Pirscher et al., 2007). GNSS-RO are then interpolated using the spring analogy (D'Errico, 2004). Subsequently, the incomplete and inconsistent radiosonde record over Africa is filled with GNSS-RO data. Finally, GNSS-RO fields are used to characterize the African tropopause and analyze tropopause variability in relation to global and regional climate drivers. Consistency checks between GNSS-RO and reanalysis products (i.e., ERA5 and MERRA-2) are carried out throughout.

2.2.1. Definition of the Tropopause Used in This Study

The tropopause is commonly defined as either the lapse rate thermal tropopause (LRT) or the cold-point tropopause (CPT). WMO (1957) defines the LRT as "the lowest level at which the lapse rate decreases to 2°C km^{-1} or less, provided also the average lapse rate between this level and all higher levels within 2 km does not exceed 2°C km^{-1}," while the CPT is the level of the minimum temperature in the region below the stratopause. The

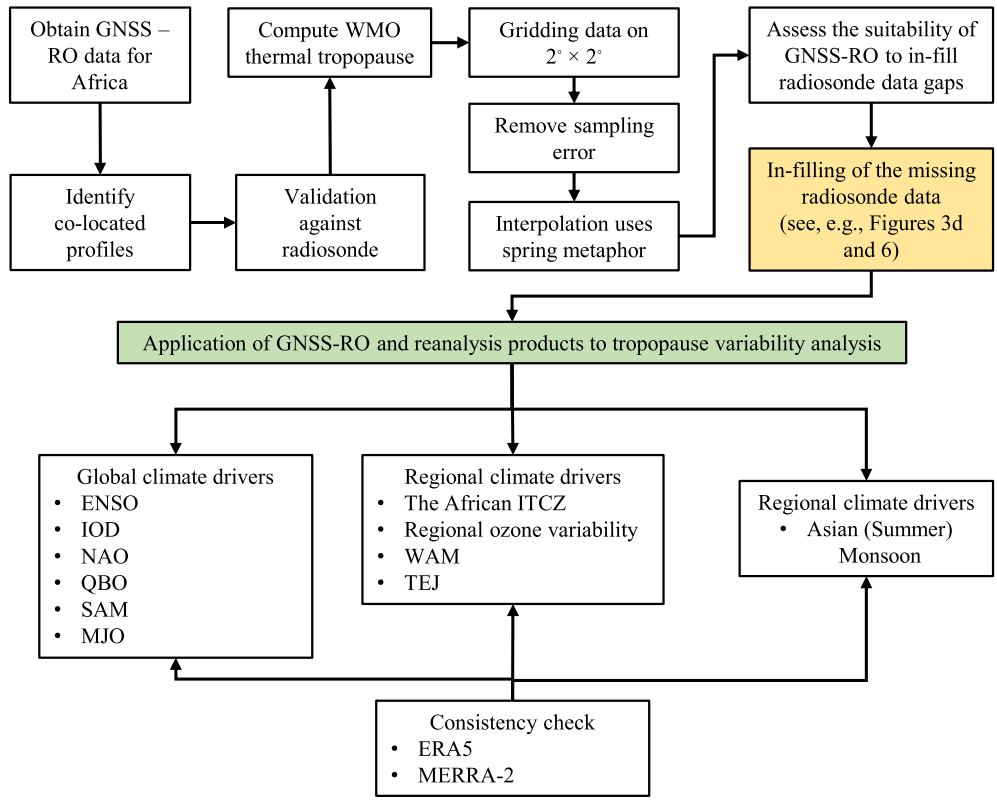

Figure 2. Schematic workflow of using Global Navigation Satellite System-Radio Occultation to address the radiosonde data gaps and investigate tropopause variability over Africa in relation to climate drivers (global and regional).

narrow layer about 1–2 km from CPT (Tropopause Inversion Layer-TIL), which represents the sharp gradient of vertical temperature profile within the tropopause, has a strong relationship with the annual cycle and interannual variability of QBO (e.g., Noersomadi et al., 2019; Randel et al., 2000), while the LRT is shown to provide more consistent results in identifying the transition from the troposphere to the stratosphere (Pan et al., 2018). Therefore, the LRT definition is applied to identify the tropopause from all data sets.

2.2.2. Validation Method

To compare GNSS-RO with in situ radiosonde data from across Africa, the mean temperature difference $\overline{\Delta T(l)}$ and the corresponding standard deviation $\sigma_{\Delta T}(l)$ are calculated at pressure levels l = 850, 700, 500, 400, 300, 250, 200, 150, 100, 70, 50, 30, and 20 hPa and at tropopause level by:

$$\overline{\Delta T(l)} = \frac{1}{M(l)} \sum_{i=1}^{M(l)} \left[T_{\mathrm{GNSS}}(i,l) - T_{\mathrm{RS}}(i,l) \right], \tag{1}$$

$$\sigma_{\Delta T}(l) = \sqrt{\frac{1}{M(l)-1} \sum_{i=1}^{M(l)} \left[T_{\mathrm{GNSS\text{-}RS}}(i,l) - \overline{\Delta T(l)} \right]^2}, \tag{2}$$

where $M(l)$ is the number of data points at the level l and T_{GNSS} and T_{RS} are the temperature from GNSS-RO and the radiosonde data, respectively (Wickert, 2004). $T_{\mathrm{GNSS-RS}}$ are the actual temperature differences between GNSS-RO and radiosonde data. Comparisons between radiosonde and GNSS-RO data are made only for profiles less than 100 km and 3 hr apart from each other (Khandu et al., 2011). Data are discarded if they exhibit a temperature difference of more than 15 K above 9 km for quality control. Differences caused by comparing GNSS-RO dry temperature and radiosonde physical temperature are usually less than 5 K above 9 km (see Scherllin-Pirscher, Kirchengast, et al., 2011). For all GNSS-RO and radiosonde profile pairs, their co-located ERA5 and MERRA-2 profiles are extracted as well and used for comparison.

Kling-Gupta Efficiency (KGE; Gupta et al., 2009) is used to measure the agreement of GNSS-RO and reanalysis products against those of the radiosonde.

$$KGE = 1 - \sqrt{(r-1)^2 + (\alpha - 1)^2 + (\beta - 1)^2}, \tag{3}$$

where r represents the correlation between GNSS-RO and radiosonde data, α is the ratio between the standard deviation of GNSS-RO and the standard deviation of radiosonde data, and β is the ratio between the mean of GNSS-RO and the mean of radiosonde data. The same procedure is applied to reanalysis products for comparison. The KGE value of 1 indicates that the comparison data sets perfectly fits the radiosonde data.

2.2.3. GNSS-RO Climatological Fields

All GNSS-RO data are monthly gridded at a spatial resolution of 2° × 2°, as an individual RO profile has on average a horizontal extension of 250 km along the ray (see, e.g., Scherllin-Pirscher et al., 2021). Due to the high consistency of GNSS-RO measurements (Angerer et al., 2017), high-quality profiles from several missions are used. GNSS-RO sampling is inhomogeneous, and as such, it includes sampling errors due to unevenly distributed observations in both time and space (Foelsche et al., 2011; Scherllin-Pirscher et al., 2007). These sampling errors are estimated using co-located ERA5 reanalysis profiles (i.e., at four times 00:00, 06:00, 12:00, and 18:00 UTC) and monthly mean ERA5 fields. The climatological difference (i.e., the sampling error) of the reanalysis products is subtracted from the GNSS-RO climatology. More details on this method can be found in Scherllin-Pirscher et al. (2007) and Foelsche et al. (2008). Empty grid boxes are filled by using a spring analogy interpolation algorithm (D'Errico, 2004). The sampling error-corrected spatially interpolated GNSS-RO fields are used for tropopause variability analysis.

2.2.4. Correlation Analysis

The instantaneous Pearson correlation coefficient is used to analyze the relationship between global climate indices and tropopause variability, (see, e.g., Anyah et al., 2018; Scherllin-Pirscher et al., 2012). First, low pass filters (i.e., order = 4; cutoff period = 12 months) are applied to African tropopause temperature and height fields to filter noise. Then, the spatial-temporal relationships between deseasonalized tropopause parameters (temperature and height) and climate indices are established. Statistically insignificant results ($p > 0.05$) are removed from the analysis.

2.2.5. Principal Components Analysis

Principal components analysis (PCA; Preisendorfer & Mobley, 1988) is applied to extract the most dominant signals explaining the majority of variability in the two-dimensional atmospheric data sets. The input data are first deseasonalized and then decomposed into modes of variability ($D_{t,s}$). Each mode n is expressed by an empirical orthogonal function (EOF) representing the spatial pattern s and a principal component (PC) describing the temporal component t:

$$D_{t,s} = \mathrm{PC}_{(t,n)}\mathrm{EOF}_{(s,n)}. \tag{4}$$

The eigenvalues' scree plot is applied to ensure that the retained EOFs represent more signal than noise, see, for example, Forootan et al. (2012, 2014).

2.2.6. Independent Component Analysis

While PCA does an excellent work in detecting major climate drivers over Africa, it lacks the robustness of the independent components analysis (ICA; Hyvärinen & Oja, 2000) needed to reveal hidden signals of the data that are not captured by PCA (see, e.g., Westra et al., 2010). ICA is a higher order (fourth-order cumulant) statistics used to solve blind source separation by assuming the sources are statistically independent in time, and contain components with non-Gaussianity which is measured by kurtosis (i.e., a fourth-order cumulants at zero time lags) (Forootan et al., 2012).

The kurtosis of the time series k is used to compute the non-Gaussianity of time series (Comon, 1994)

$$k = \frac{E\left(x^4\right)}{E(x^2)^2} - 3, \tag{5}$$

where x represents each time series and E is the expectation function such as time average. Since regional climate drivers have assertive intraseasonal and interseasonal behavior that are not captured by PCA, ICA is applied to raw data to separate the seasonality link with the regional climate indices.

3. Results and Discussion

3.1. Potential of GNSS-RO to Infill Missing Radiosonde Data

3.1.1. Analysis of the State of Radiosonde Data Over Africa

This study shows an alarming reduction in the number of radiosonde stations over the past decades in Africa (see Figure 3a, shown in gray). Since the 1980s, roughly 50 stations have been deactivated per decade, leading to a depletion of approximately 300,000 observations per decade. There are currently only 50 radiosonde stations left that operationally perform measurements in 26 African countries. The rest of the countries reported no active radiosonde stations by 2020 (see Figure 3b). Observations are predominately reported from specific regions (e.g., South Africa, the coastal rim of Northern Africa), but rarely from Central Africa and East Africa. Due to missing, problematic, and low-quality data, only 42 stations from 23 countries were used for validation in this study (see Figure 3b and 3c). This means that approximately 57% of all African countries have no direct access to upper-air information from radiosonde stations. The minimum number of daily observations does not meet the WMO recommendations to study daily variations caused by diurnal and semidiurnal tides (see https://library.wmo.int/doc_num.php?explnum_id=3158).

This study used a total of 432,239 observations since May 2001. From the active stations, 165,775 measurements were missing or incomplete, and 51,333 were of low quality, accounting for 38% and 12% of the data, respectively. Most high-quality measurements were provided by Algeria, Egypt, and South Africa. While some countries only provide very few high-quality measurements (e.g., Morroco, Nigeria, Seychelles, and Western Sahara), the percentage of high-quality measurements is low, for example, in Benin, Congo Republic, and Madagascar (see Figure 3c). Moreover, this study found 38% of the radiosonde records include missing data, and approximately 57% of all African countries have had several years without any operational radiosonde launches. Despite there being 23 African countries that reported radiosonde measurements in 2020, 14 of them kept less than 50% of radiosonde records from 2001 to 2020, accounting for 25% of all African countries. Overall, 82% of African countries are either experiencing severe radiosonde data gaps (57%) or have had data gaps in the past two decades (25%), which is now infilled in Figure 3d. On the other hand, the use of GNSS-RO measurements from 2001 onward and, in particular, the high number of COSMIC-2 profiles available since 2019 can mitigate the significant reduction of radiosonde data (see Figure 3d).

3.1.2. Statistical Comparison and Validation of GNSS-RO Against Radiosonde and Reanalysis Products

Figure 4 shows 12 radiosonde temperature profiles together with their co-located profiles from several GNSS-RO missions and reanalysis products. These profiles are selected to exemplify some characteristics representative of many other profiles. In general, the data sets show an almost identical behavior for the atmosphere between 8 and 25 km, with the GNSS-RO products having a sharper, explicit feature in the UTLS region, whereas both ERA5 and MERRA-2 show a rather smooth behavior due to their lower vertical resolutions. Profiles from Tamanrasset in Algeria (22.80°N, 5.43°E; Figure 4b), the Ivato International Airport in Madagascar (18.80°S, 47.48°E; Figure 4d), and Cape Town in South Africa (33.97°S, 18.60°E; Figure 4l) are examples that show the smooth spline used by the reanalysis products. In addition, Figure 4g and 4h show that both reanalyses sometimes misidentify the tropopause and in some cases, the reanalysis products do not capture the tropopause inversion layer (e.g., Farafra in Egypt (Figure 4a), Nouakchott in Mauritania (Figure 4e), Pointe-Noire in Congo Republic (Figure 4h), and Tunis-Carthage in Tunis (Figure 4k)). On the other hand, GNSS-RO measurements from all satellites are in good agreement with radiosonde data. This is a promising result considering that GNSS-RO data can be used to fill the radiosonde data gaps above Africa.

Figure 5 presents the overall statistical validation of the co-located GNSS-RO profiles with high-quality and complete vertical profiles from radiosonde soundings for the African continent for the period 2001–2020,

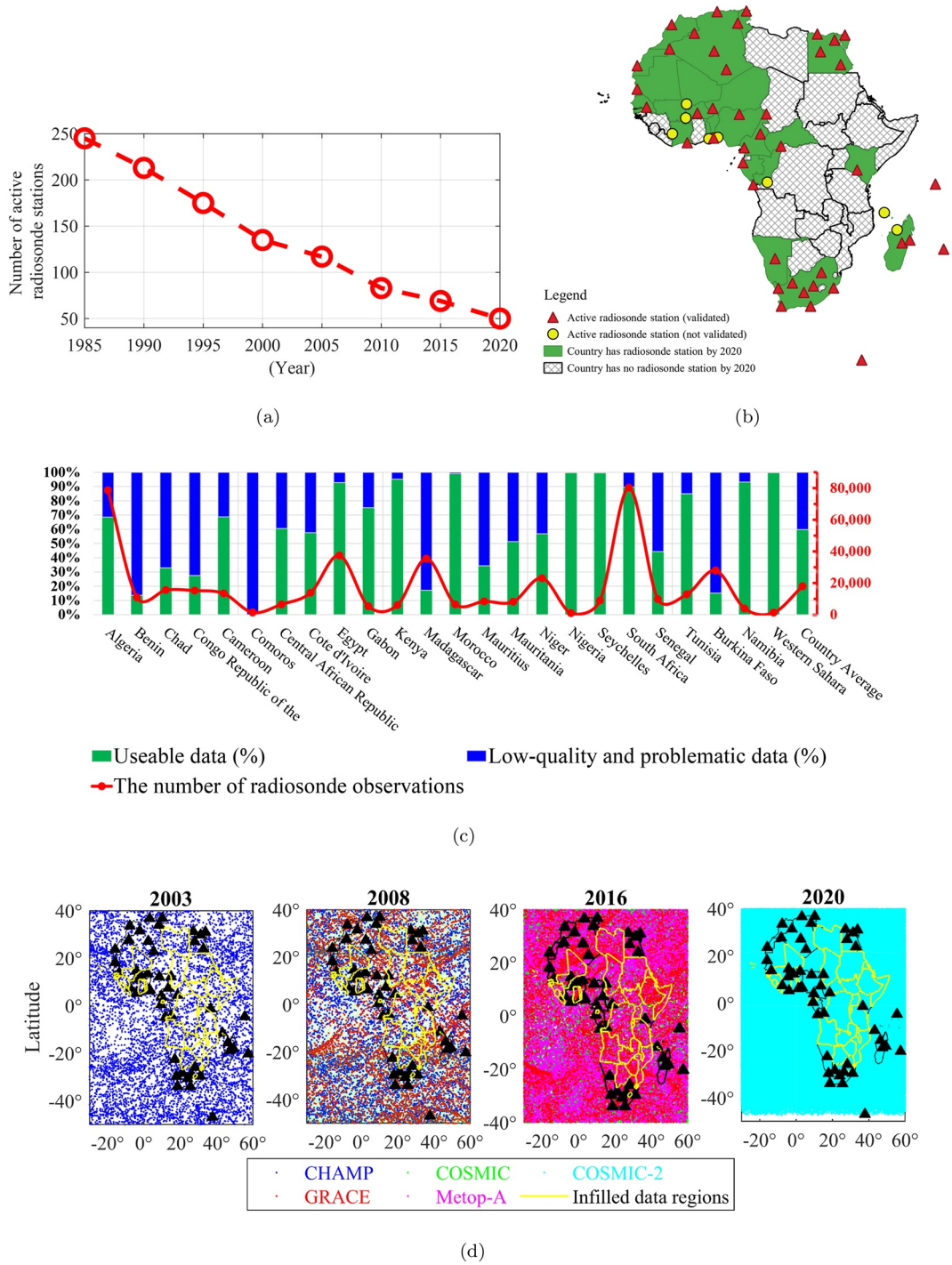

Figure 3. (a) The number of operational radiosonde stations in Africa from 1985 to 2020, (b) availability of radiosonde stations over the African continent by 2020 showing countries with operational radiosonde stations in 2020 (green) and those without operational radiosonde stations in 2020 (gray), (c) Percentage of high- (green) and low-quality (blue) measurements from 2000 to 2020 as well as total number of soundings per country (the red line), and (d) Global Navigation Satellite System-Radio Occultation data coverage in 2003, 2008, 2016, and 2020.

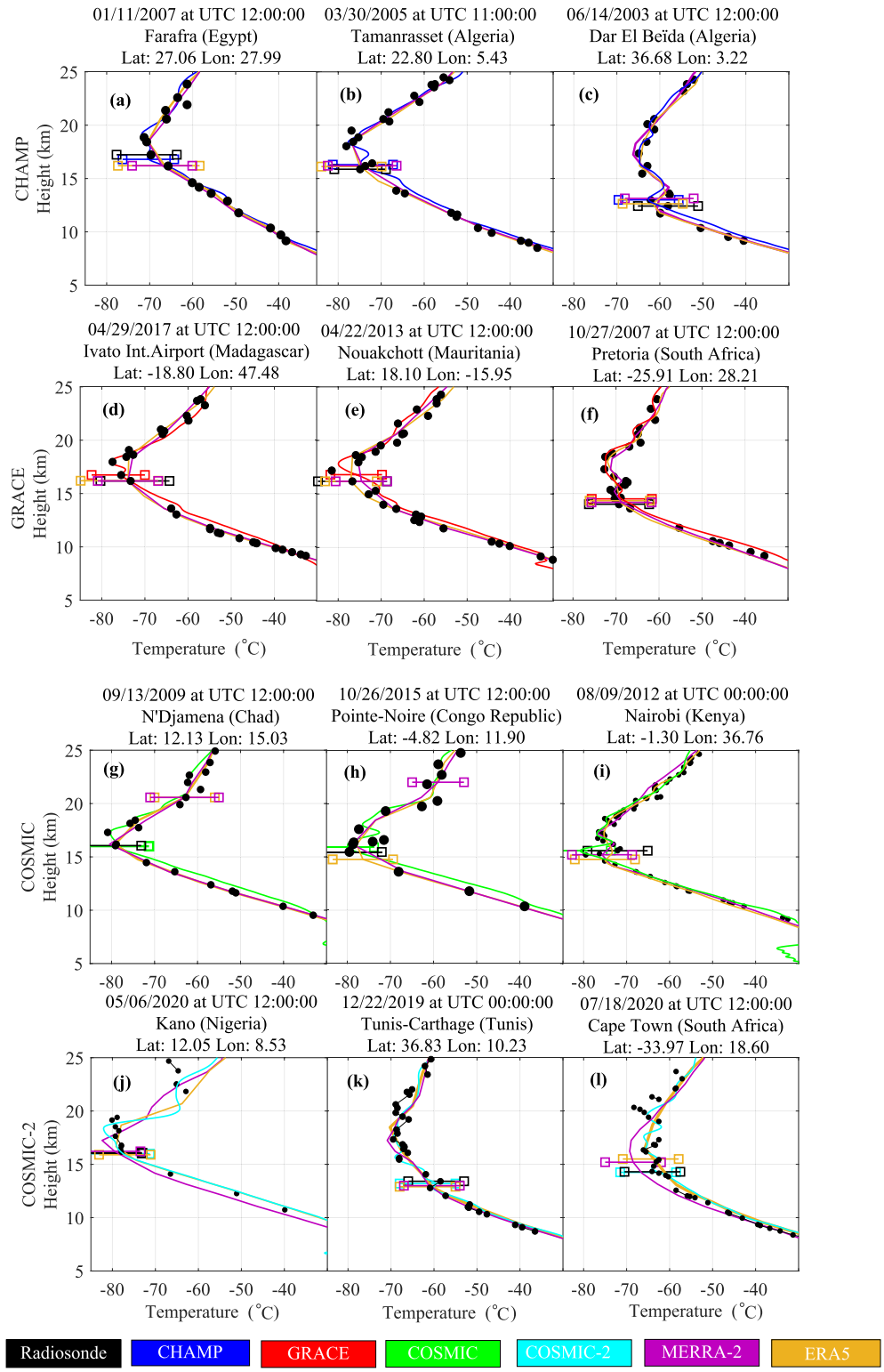

Figure 4. Radiosonde soundings and co-located (within 100 km and 3 hr) reanalysis profiles as well as Global Navigation Satellite System-Radio Occultation measurements from (a–c) Challenging Mini-satellite Payload, (d–f) Gravity Recovery and Climate Experiment, (g–i) Constellation Observing System for Meteorology, Ionosphere, and Climate (COSMIC), and (j–l) COSMIC-2. Details about the radiosonde measurements, that is, time of the observation, location with latitude and longitude, and provider country in bracket are given in the panel titles. Horizontal lines indicate the location of the tropopause of each profile.

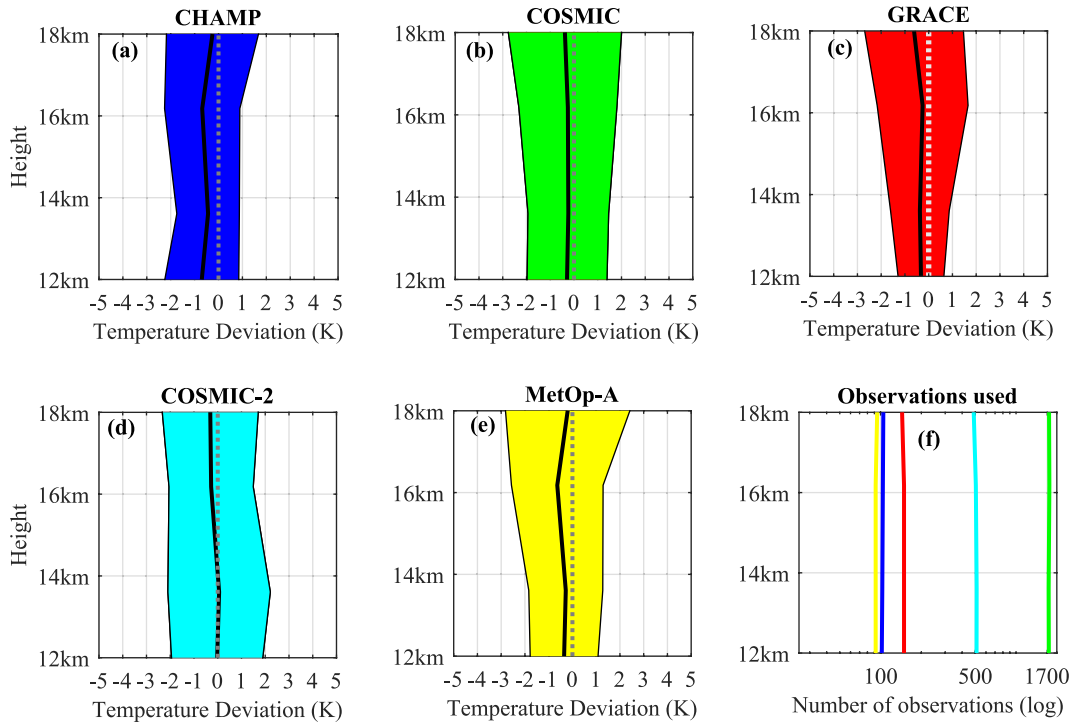

Figure 5. Mean temperature difference (thick black lines) and standard deviations (colored areas) between African radiosonde measurements and (a; blue) Challenging Mini-satellite Payload, (b; green) Constellation Observing System for Meteorology, Ionosphere, and Climate (COSMIC), (c; red) Gravity Recovery and Climate Experiment, (d; cyan) COSMIC-2, and (e; yellow) Meteorological Operational satellite-A. (f) The number of observations used for validation at each geopotential height level.

including 109 CHAMP, 150 GRACE, 1,942 COSMIC, 91 MetOp-A, and 528 COSMIC-2 profiles. Between 12 and 18 km, the GNSS-RO data have a mean temperature difference to African radiosonde measurements of −0.53 K (CHAMP; Figure 5a), −0.28 K (COSMIC; Figure 5b), −0.37 K (GRACE; Figure 5c), −0.14 K (COSMIC-2; Figure 5d), and −0.40 K (MetOp; Figure 5e).

The Vaisala RS80 (without a GPS receiver onboard) and RS92 (with a GPS receiver onboard) were the primary radiosonde types used in Africa, which have a mean temperature difference with GNSS-RO of 0.10 ± 1.54 K and 0.16 ± 1.54 K from 200 to 20 hPa, respectively (Ho et al., 2017; Inai et al., 2015). Radiosonde errors are attributable to sensor-dependent biases such as uncorrected radiation biases and changes of radiation correction table, and they range from 0.1 to 0.5 K and 0.1 to 0.15 K, respectively. Applying sensor radiation correction to radiosonde data is solely dependent on the operating organization. Moreover, the radiosonde bias varies among different locations and methodology for determining the tropopause (Staten & Reichler, 2008). The Vaisala RS80 has a pressure bias of 43 ± 23 m at the geopotential height of 20 km, while the Vaisala RS92 radiosonde has a geopotential height bias of 10–50 m and those manufactured prior to 2004 have a systematic pressure difference of up to ±100 m at higher altitudes (Dirksen et al., 2014; Inai et al., 2015; Steinbrecht et al., 2008). Larger errors are expected in radiosonde data if the amount of air injected into the balloon is inadequate (Dirksen et al., 2014). In addition, the quality of radiosonde data changes from time to time due to discontinuity of measurement in the vertical profile, inconsistent instrument practices, lack of instrumental calibration, and incorrect sensor correction. These random uncertainties of radiosondes were challenging to eliminate and quantify (see Dirksen et al., 2014), which alters the characteristics of vertical profiles from the radiosondes. It is worthy to note that the radiosonde data sets used in this study (i.e., IGRA) documented inconsistencies (Staten & Reichler, 2008). On the other hand, the GNSS biases in the UTLS are small (see e.g., Ho et al., 2017; Kuo et al., 2005; Scherllin-Pirscher, Steiner, et al., 2011). For instance, Scherllin-Pirscher et al. (2017) discussed the error characteristics of the tropopause parameters of GNSS-RO data. At low latitudes, the bias of tropopause parameters was estimated at 0.1 K for temperature and 0.1% for pressure. A total error of tropopause temperature and pressure at low latitudes

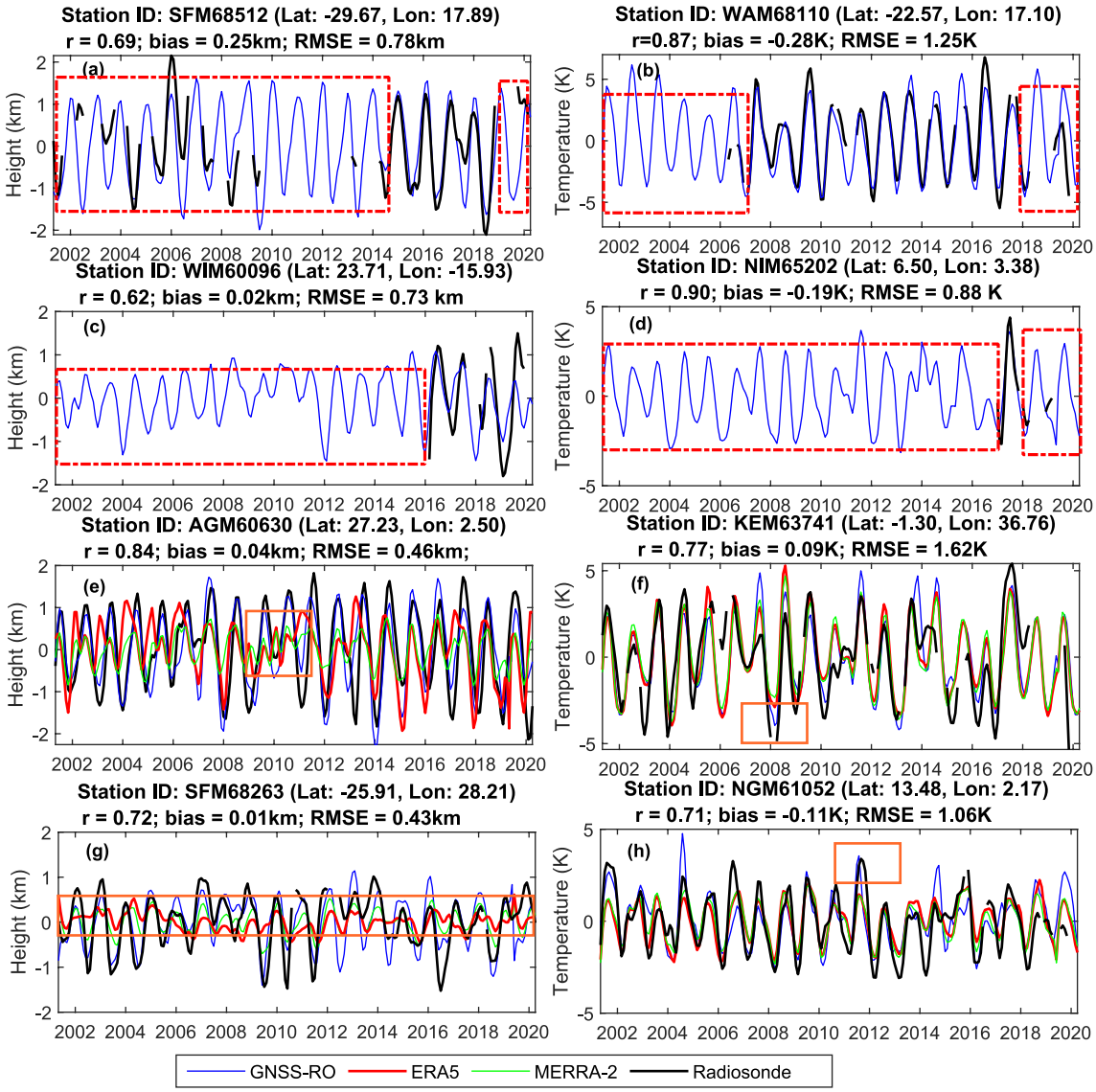

Figure 6. Time series of tropopause height anomalies (left panels) and tropopause temperature anomalies (right panels) from 2001 to 2020 for eight African stations from radiosonde measurements (black), Global Navigation Satellite System-Radio Occultation (GNSS-RO) (blue), European Centre for Medium-Range Weather Forecasts Reanalysis 5 (red), and Modern-Era Retrospective analysis for Research and Applications version 2 (green). Red dashed boxes in panels (a–d) indicate long radiosonde data gaps due to missing, incomplete, or low-quality data, which are infilled using GNSS-RO. Orange boxes in panels (e–h) indicate time periods with larger differences between reanalyses and radiosondes. The panel titles contain radiosonde stations' country code, station code, latitude, and longitude. The panel titles also provide statistical measures, for example, correlation coefficient (r), bias, and root mean square error.

amounts to 0.15 K and 0.1 hPa. Therefore, it is reasonable to suggest that the quality of GNSS-RO is good, and it is able to infill the radiosonde data gap over Africa.

3.1.3. The Suitability of GNSS-RO Data to Infill Radiosonde Data Gaps

Figures 6a–6d show examples of GNSS-RO infilling of the radiosonde data gaps for some stations with long data gaps in the UTLS region due to problematic radiosonde measurements. The full time series of GNSS-RO data are obtained from observation, which has been gridded using our method (see Section 2.2.3). Radiosonde stations were launched decades ago (e.g., the South African station SFM68512 was launched in 1987 (Figure 6a), WAM68110 (Namibia; Figure 6b) in 1986, WIM60096 (Western Sahara; Figure 6c) in 1974, and NIM65202 (Nigeria; Figure 6d) in 1966). Tropopause height and temperature anomalies are calculated by subtracting the long-term mean of each data set. Overall, GNSS-RO performs well in addressing the radiosonde data gaps.

Table 2
Bias, Correlation Coefficient r, and Root Mean Square Error of Challenging Mini-Satellite Payload, Gravity Recovery And Climate Experiment, Constellation Observing System for Meteorology, Ionosphere, and Climate (COSMIC), COSMIC-2, Meteorological Operational Satellite-A, Global Navigation Satellite System-Radio Occultation, European Centre for Medium-Range Weather Forecasts Reanalysis 5, and Modern-Era Retrospective Analysis for Research and Applications version 2 Tropopause Height and Tropopause Temperature Relative to the Consistent Record From High-Quality African Radiosonde Measurements

	Tropopause height (km)			Tropopause temperature (K)			No. of data
	Bias	*r*	RMSE	Bias	*r*	RMSE	
CHAMP	0.12	0.86	0.58	−0.26	0.89	1.04	87
GRACE	0.11	0.86	0.69	−0.23	0.87	1.15	103
COSMIC	0.03	0.94	0.28	−0.12	0.93	0.63	1,263
COSMIC-2	0.04	0.90	0.34	−0.16	0.90	0.82	378
MetOp-A	0.08	0.83	0.46	−0.22	0.88	1.16	33
GNSS-RO	0.04	0.86	0.37	−0.21	0.91	0.85	228
ERA5	0.05	0.83	0.45	−0.37	0.87	0.98	228
MERRA-2	0.09	0.81	0.67	−0.39	0.86	1.03	228

Figures 6e–6h reveal issues regarding attempts to use reanalysis products to infill the radiosonde data gaps over Africa. When used to infill, both reanalysis products (MERRA-2 and ERA5) sometimes perform poorly in capturing the interannual variation of tropopause height, see for example, Figures 6e and 6g.

In Table 2, the tropopause properties derived from CHAMP, GRACE, COSMIC, COSMIC-2, and MetOp-A are assessed against those derived from good quality co-located radiosonde profiles within 100 km^{-3} hr. This comparison was constructed over a continental scale. Moreover, we randomly selected one sample of co-located GNSS-RO data (i.e., regardless of missions) from each month over the time spanning of this study (i.e., 228 months in total) and their spatially and temporally correspondent gridded data in reanalyses to evaluate their quality compared to radiosonde data. This comparison was constructed on data collected from Algeria, Egypt, Morocco, and South Africa. The bias indicates whether data overestimate or underestimate tropopause properties, and the correlation coefficient (r) shows the overall consistency. The root mean square error (RMSE) estimates the goodness of fit. The best quality of individual GNSS-RO missions relative to radiosonde data is found of the COSMIC and COSMIC-2 missions. For combined GNSS-RO data and reanalysis products relative to radiosonde, we found that both reanalyses and GNSS-RO tend to overestimate tropopause height and underestimate tropopause temperature. Second, reanalyses' and GNSS-ROs' data sets have a strong correlation coefficient with radiosonde data, indicating good overall consistency. The GNSS-RO has the best RMSE value of tropopause heights (0.37 km) and tropopause temperature (0.85 K), followed by ERA5 and MERRA-2. Therefore, for the tropopause properties analysis, the overall result suggests that GNSS-RO data should be prioritized for use when available. At the same time, reanalyses can complement the radiosonde data gaps when unable to access GNSS-RO.

Figure 7 shows the performance of co-located GNSS-RO vertical profiles and reanalyses relative to good quality radiosonde measurements. Towner et al. (2019) suggests that KGE values of 0.75 or higher indicate a good agreement between observations and simulated products, and KGE values lower than 0.5 are considered "bad" (Andersson et al., 2017). In general, the GNSS-RO outperforms reanalysis products, with KGE values being higher than ERA5 and MERRA-2 at all height levels, indicating the advantage of GNSS-RO to infill the radiosonde data gaps in the UTLS region. Figures 7b and 7c show the performance of decades-long time series derived from GNSS-RO data and reanalysis products relative to radiosonde records in both tropopause heights and temperatures of individual countries. Given lower KGE values, the plot reveals that many countries suffer from poor long-term radiosonde records in the UTLS, for example, BN (Benin), MR (Mauritania), and CD (Chad) (see Section 3.1.1). Noticeably, the data quality of tropopause heights is lower than that of tropopause temperature, which is possibly attributable to a radiosonde pressure bias discussed in Section 3.1.2 (e.g., non-GPS Vaisala RS80 radiosonde) (Inai et al., 2015). Higher KGE values in tropopause heights and temperatures are found in Algeria, Egypt, Morocco, and South Africa. In contrast, radiosonde stations from other countries lack quality. As a whole, Figures 7b and 7c indicate that about 78% of the countries had their height profiles' KGE and 57% of

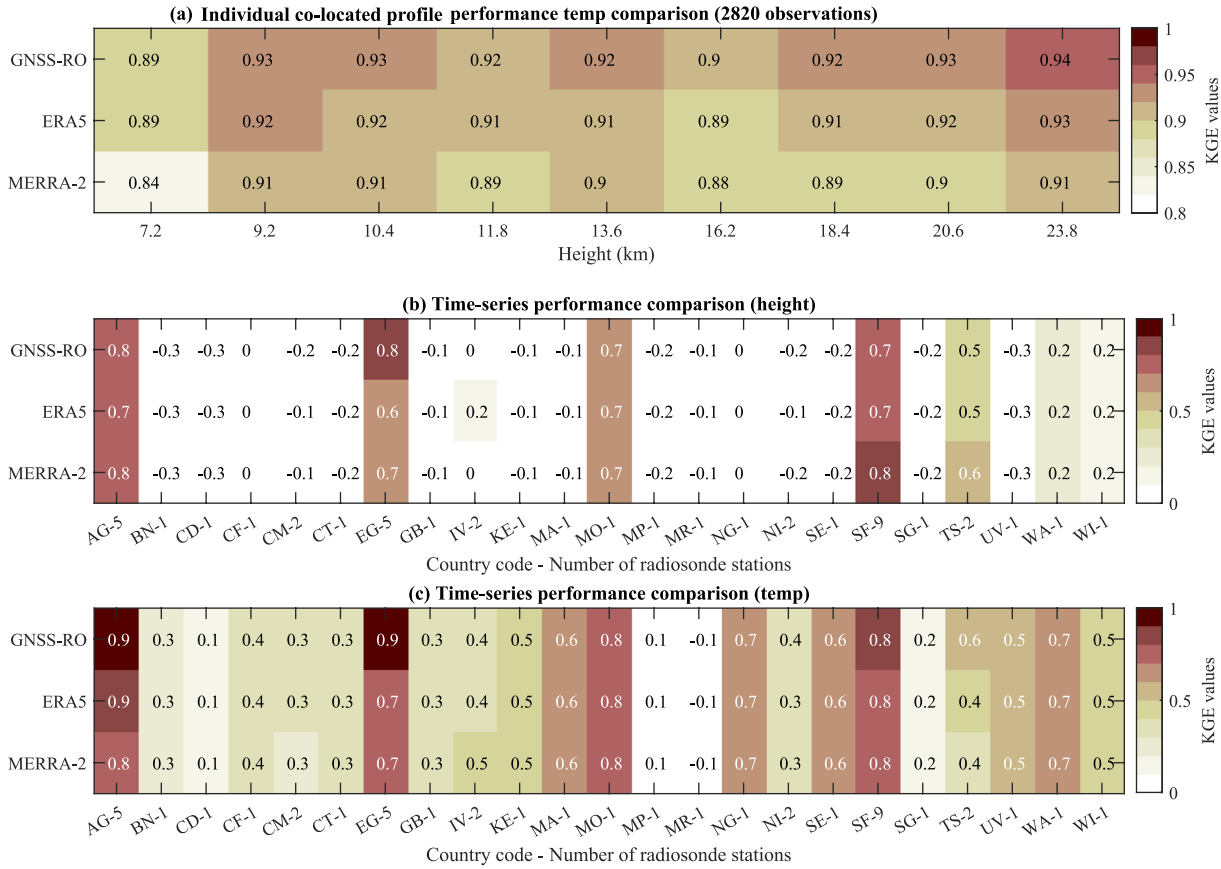

Figure 7. (a) Kling-Gupta efficiency (KGE) values of vertical profiles from reanalyses and Global Navigation Satellite System-Radio Occultation (GNSS-RO) against good radiosonde observations at different heights. The mean KGE values are 0.92 (GNSS-RO), 0.9 (European Centre for Medium-Range Weather Forecasts Reanalysis 5), and 0.89 (Modern-Era Retrospective analysis for Research and Applications version 2), (b) the KGE values for time series of tropopause heights, and (c) temperatures based on reanalysis products and GNSS-RO against radiosonde records. The *x* axes show the country code and the number of radiosonde stations used. Information for the country code is provided in Supporting Information S1. KGE values lower than 0.5 indicate countries with unreliable radiosonde data (e.g., Figure 3c; Andersson et al. (2017)).

temperature profiles' KGE less than 0.5. These corroborate the findings of Section 3.1.1 that indicated that about 80% of the African countries lacked radiosonde data while 57% suspended their radiosonde stations prior to 2020 and 25% of countries have more than 50% missing radiosonde data, highlighting the importance of GNSS-RO products to the data deficient Africa. In general, the ongoing developments in GNSS-RO remote sensing to obtain full coverage over the continent by providing consistent measurements simultaneously are essential to preserving the valuable source of atmosphere observations for Africa. More importantly, GNSS-RO provides real-time observations, and data become available in near-real-time, while ERA5 is updated daily but with a latency of 5 days. GNSS-RO can provide more than 1.5 million accurate and consistent atmospheric vertical profiles for data-deficient Africa, which is not achievable using radiosonde measurements alone.

3.1.4. Spatiotemporal Characteristics of the African Tropopause

Figure 8 presents the area-averaged temporal variability of the tropopause height (Figures 8a–8d) and temperature (Figures 8e–8h) of GNSS-RO measurements and reanalysis products in four geographical regions. A consistent seasonal variation is found for all data sets. However, the reanalysis products uniformly show a lower tropopause height than GNSS-RO (see Figures 8a–8d) with largest differences at tropical latitudes. Tropopause temperature is, in general, in better agreement among the data sets with a small positive bias of the reanalysis products (see Figures 8e–8h). This bias is possibly caused by the reanalyses coarser vertical resolution. This behavior is consistent with a recent study by Meng et al. (2021), who found a global mean pressure bias of −0.9 hPa in MERRA-2, attributable to a large bias over the subtropics in December-January-February and June-July-August (JJA). Similarly, Tegtmeier et al. (2020) showed that MERRA-2 and ERA5 exhibit a warm bias ranging from

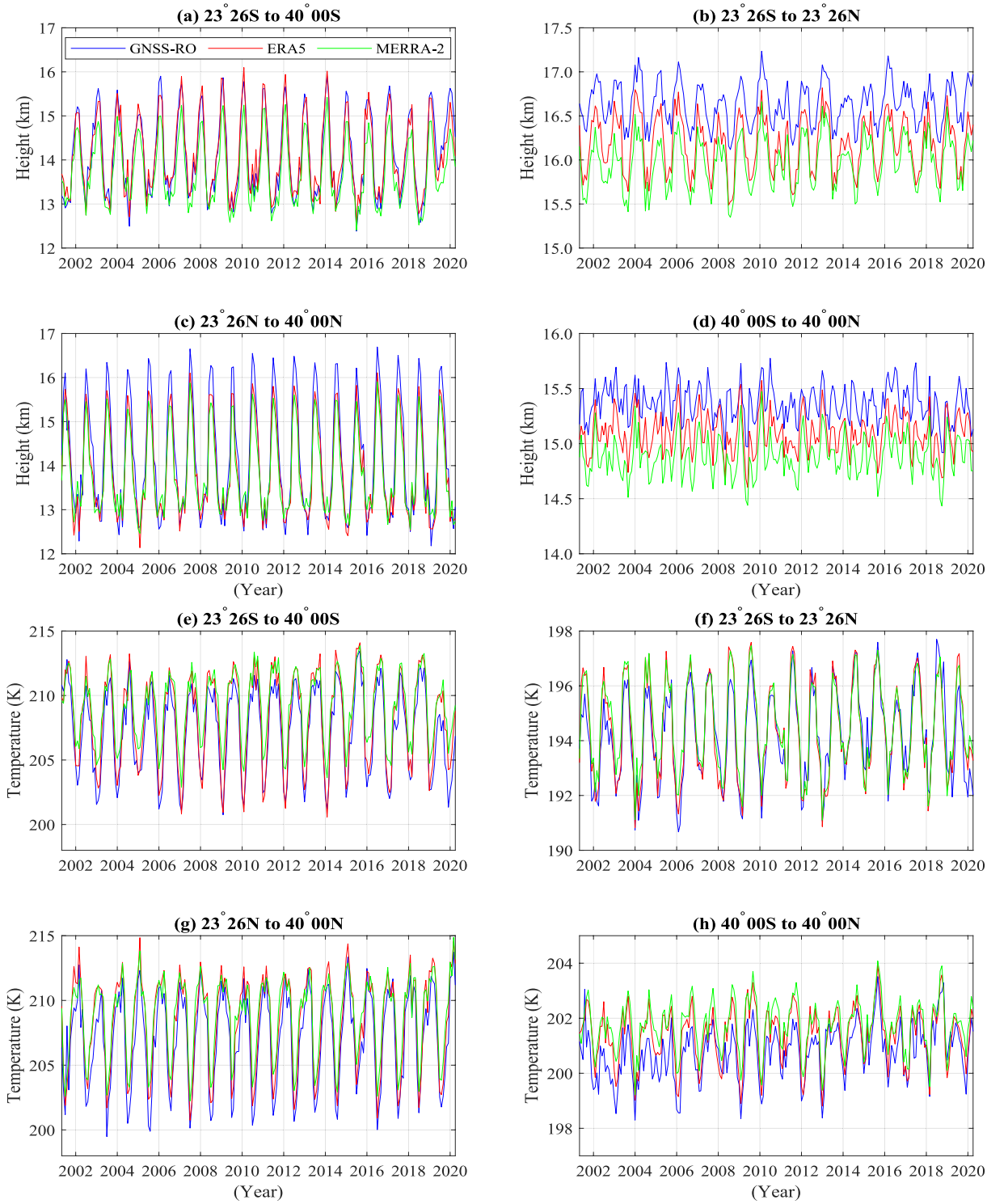

Figure 8. Temporal evolution of (a–d) tropopause heights and (e–h) temperatures from Global Navigation Satellite System-Radio Occultation and reanalysis products in southern subtropics (23°26'S–40°00'S), tropics (23°26'N–23°26'S), northern subtropics (23°26'N–40°00'N), and over entire Africa (40°00'S–40°00'N). (d) and (h) are the area-weighted means of panels (a–c) and panels (e–g), respectively. The east-west extension is the same for all areas and corresponds to the extent of the study area.

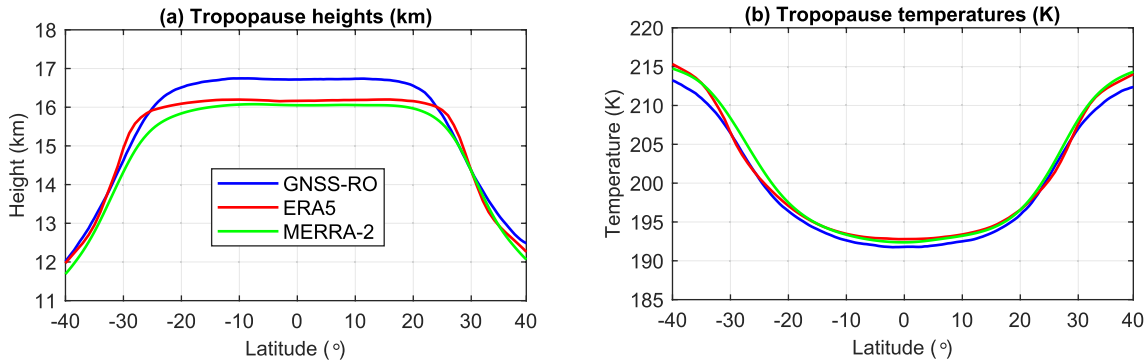

Figure 9. Latitudinal variation of the long-term mean (2001–2020) (a) tropopause height and (b) temperature from Global Navigation Satellite System-Radio Occultation, European Centre for Medium-Range Weather Forecasts Reanalysis 5, and Modern-Era Retrospective analysis for Research and Applications version 2.

0.2 to 1.5 K over the tropics. In this study, the tropopause temperature based on ERA5 and MERRA-2 indicates a warm bias of 0.8 and 1.2 K, respectively. ERA5 and MERRA-2 tropopause heights are negatively biased by 0.3 and 0.5 km, respectively. Thus, ERA5 is generally in better agreement with GNSS-RO than MERRA-2. The reanalysis products indicate clear improvements after being deseasonalized and detrended. The mean difference between GNSS-RO and reanalyses reduces to less than 0.02 km and 0.02 K for height and temperature, respectively, and the primary cause of the seasonal bias is the underestimation of seasonal amplitude.

The long-term mean tropopause height and temperature with respect to latitude are presented in Figure 9. The bias of the reanalyses tropopause heights is again clearly seen at tropical latitudes (23°S–23°N). From 10°S–10°N, this bias amounts to 0.5–0.6 km. Poleward of 30°S, ERA5 is in good agreement with GNSS-RO but MERRA-2 tropopause height is negatively biased (0.4 km). Poleward of 30°N, however, GNSS-RO tropopause height is higher than that of ERA5 and MERRA-2 by 0.2 and 0.3 km, respectively. The temperature bias of MERRA-2 increases from 0.7 K at tropical latitudes (10°S–10°N) to 1.8 K at extratropical latitudes (poleward of 30°N/S). Differences between ERA5 and GNSS-RO remain within 0.8 K at tropical latitudes. Poleward of 30°N/S, ERA5 tropopause is biased by 1.5 K.

3.2. Variability of the African Tropopause in Relation to Climate Drivers

3.2.1. Variability in Relation to Global Climate Drivers

Figure 10 shows the correlation (at zero lag) between six global climate driver indices (i.e., ENSO, MJO, NAO, SAM, IOD, and QBO) and deseasonalized time series of tropopause heights and temperatures for the period of 2001–2020 estimated using GNSS-RO and reanalysis products. Deseasonalization is to highlight long-term variations. The table embedded in Figure 10 summarizes the relationship between global climate drivers and tropopause parameters for several African regions.

In general, reanalyses and GNSS-RO reveal similar correlation patterns with these six climate drivers. A connection between tropopause parameters and ENSO is found over most of the African continent. The atmospheric ENSO signal is stronger in tropopause temperature than in tropopause height. Both exhibit a rather zonally symmetric structure with that of tropopause temperature being strongest over the subtropical regions (i.e., 10°S/N–28°S/N). Tropopause height/temperature shows a negative/positive correlation over Northern Africa, Western Africa, and Southern Africa (see Figures 10A1–10F1). Other strong ENSO signals with opposite signs are observed over the Southern Ocean and close to Morocco and Algeria. These results are in good agreement with previous studies, for example, Rieckh et al. (2014). To better understand these correlations, we calculated the correlations between the ENSO index and tropopause parameters at a lag of 0, 3, and 6 months (for detailed information, see the Supporting Information S1). We found that interannual tropopause temperature anomalies show the strongest signal at a lag of 0 months. The spatial pattern of this signal is in good agreement with the eddy ENSO signal (i.e., local response, calculated as deviations from the zonal-mean, see Scherllin-Pirscher et al., 2012), which features a warming signal above Africa at tropopause altitudes (see top panel of Figure 2 of Scherllin-Pirscher et al., 2012). The signal is linked to hydrostatic horizontal pressure gradients associated with convective activity. The fast atmospheric response is related to local heating induced by positive sea surface

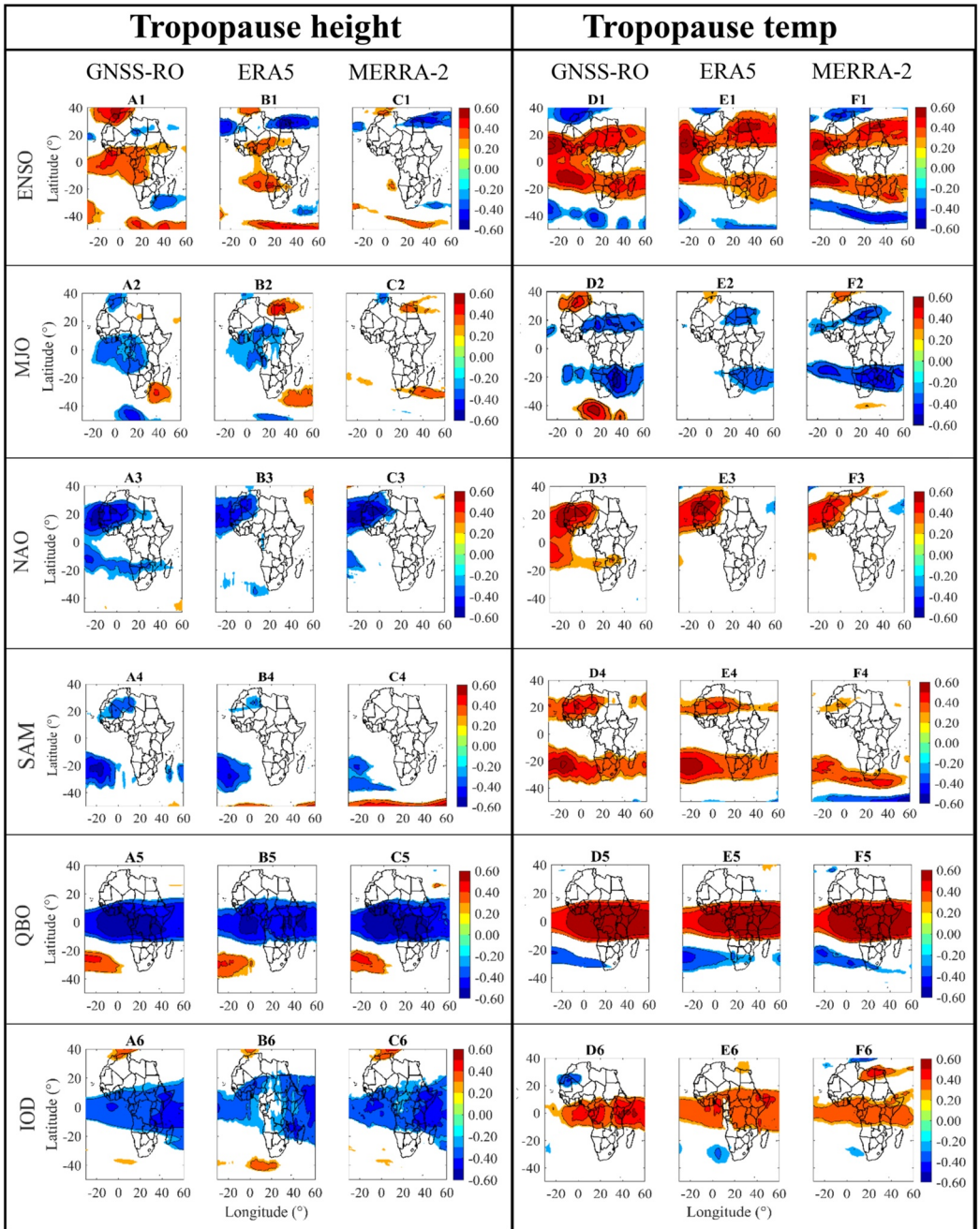

G

Drivers	ENSO		MJO		NAO		SAM		QBO		IOD	
Parameters	H	T	H	T	H	T	H	T	H	T	H	T
Northern Africa	0.4	−0.4	−0.3	0.3			−0.3	0.3				
Western Africa		0.5			−0.4	0.4			−0.4	0.4	−0.3	
Central Africa	0.4		−0.3						−0.5	0.6	−0.3	0.4
Eastern Africa		0.4							−0.4	0.6	−0.4	0.4
Southern Africa	−0.3	0.5	0.3	−0.4				0.4				

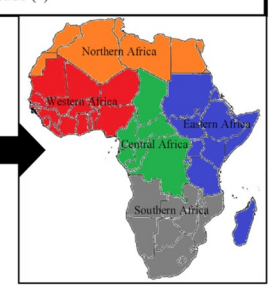

Figure 10.

temperature anomalies. In contrast to tropopause temperature, interannual tropopause height anomalies show the strongest signal at a lag of 6 months. This signal is also captured by PCA (see Figure 11). The spatial pattern of this signal is in good agreement with the zonal mean ENSO signal, which exhibits a warming throughout the tropical troposphere and a cooling in the lower stratosphere (see e.g., top panel of Figure 3 of Scherllin-Pirscher et al., 2012). This rises tropopause height and causes the positive correlation with the ENSO index. At a lag of 0 months, this signal is weak and zonal-symmetry not well pronounced yet (shown in Figure 10).

The MJO signal has a similar pattern to that of ENSO but with an opposite sign (e.g., anti-correlation) and weaker correlation (see Figures 10A2–10F2). The correlation signal between tropopause temperature and MJO appears to propagate eastward, which is consistent with Virts and Wallace (2014), who examined MJO-related variations in temperature, circulation, clouds, and trace gases at the tropical tropopause layer (TTL) and showed that as MJO convection dissipates over the tropics (Africa), it leads to zonally symmetric equatorial cold temperature anomalies, increased upwelling, and associated low ozone mixing ratios in the TTL. The temperature within the tropopause also influences the penetration of deep convection in Africa (Gettelman & Birner, 2007). Over Africa, this negative correlation between MJO and tropopause temperature and heights suggest that the negative (positive) anomalies of tropopause height and temperature move with the eastward propagation of MJO-related enhanced (suppressed) convective activities (Zeng et al., 2012). Furthermore, we extracted the mean of overlapping regions in the tropopause temperature fields with statistically significant signals from ENSO and MJO. We found excellent agreements across three representatives (i.e., MJO, ENSO, and tropopause temperature) that suggested persistent physics and chemistry interaction of ENSO (reduces hydrostatic horizontal pressure gradients during La Niña) and MJO (slows the motion of eastward convective activities) (Zeng et al., 2012), amplifying the deep convective activities on interannual time scale over Africa (see Figures 10D1–10F1 and 10D2–10F2) (Moon et al., 2011).

Tropopause height/temperature and NAO are also negatively/positively correlated over West Africa (see Figures 10A3–10F3). However, correlation between SAM and tropopause parameters indicates a weak coherence among them over Western Africa (see Figures 10A4–10F4). Stronger correlations with temperature are observed over the South Atlantic and Southern African regions, where SAM shows a positive correlation with tropopause temperature (see Figures 10D1 and 10D4). The spatial overlap of SAM and ENSO correlation with tropopause temperature suggests that both SAM and ENSO influence the tropopause over Southern Africa. This finding was also observed by previous studies (i.e., Fogt & Bromwich, 2006; L'Heureux & Thompson, 2006). For instance, Fogt et al. (2011) suggest that SAM modulates the strength of ENSO in SH extratropics.

Over the tropics, QBO and tropopause height/temperature reveal a high negative/positive correlation (see Figures 10A5–10F5). This signal is consistent with previous studies (e.g., Randel et al., 2000; Rieckh et al., 2014). Another weaker signal with opposite polarity is found in the Atlantic Ocean west of South Africa. The IOD signal has a very similar pattern to the QBO signal. Over equatorial Africa, it reveals a strong negative correlation with tropopause height (Figures 10A6–10C6) and a positive correlation with temperature (Figures 10D6–10F6).

The interannual variability of the tropopause and its relation to global climate drivers are further studied by decomposing the tropopause temperature and height fields using PCA. PCA derives the most dominant global climate drivers over Africa by finding the greatest amount of variance within the original data sets. The oceanic regions are masked to capture only the influence of climate variability of tropopause characteristics over land. The correlation between PC time series and climate indices are only discussed for statistically significant results ($p < 0.05$). The first three dominant EOFs and PCs are presented in Figures 11 and 12; the remaining are not shown as they are likely to contain more noise than signal. Figure 13 summarizes correlation coefficients and lags where maximum correlation is obtained.

ENSO is the primary driver of tropopause height variability as revealed by the correlation between the first PC time series and the ENSO index. EOF1 accounts for 39%, 47%, and 40% of variance for GNSS-RO, ERA5, and MERRA-2, respectively (Figure 11), which shows a homogeneous positive pattern over Africa. The time-lagged

Figure 10. Correlation (at zero lag) between six global climate drivers (El Niño-Southern Oscillation, Madden-Julian Oscillation, North Atlantic Oscillation, Southern Annular Mode, Quasi-Biennial Oscillation, and Indian Ocean Dipole) and tropopause heights (the left column) and temperatures (the right column) from Global Navigation Satellite System-Radio Occultation (GNSS-RO) (columns A and D), European Centre for Medium-Range Weather Forecasts Reanalysis 5 (columns B and E), and Modern-Era Retrospective analysis for Research and Applications version 2 (columns C and F) for 2001–2020. The correlations are presented if the region's tropopause variability responds to the climate driver with statistically significant results ($p < 0.05$). The table beneath the figure shows the linkage between global climate drivers and tropopause height (H) and temperature (T) from GNSS-RO data above Africa. These regions are defined in the bottom-right panel.

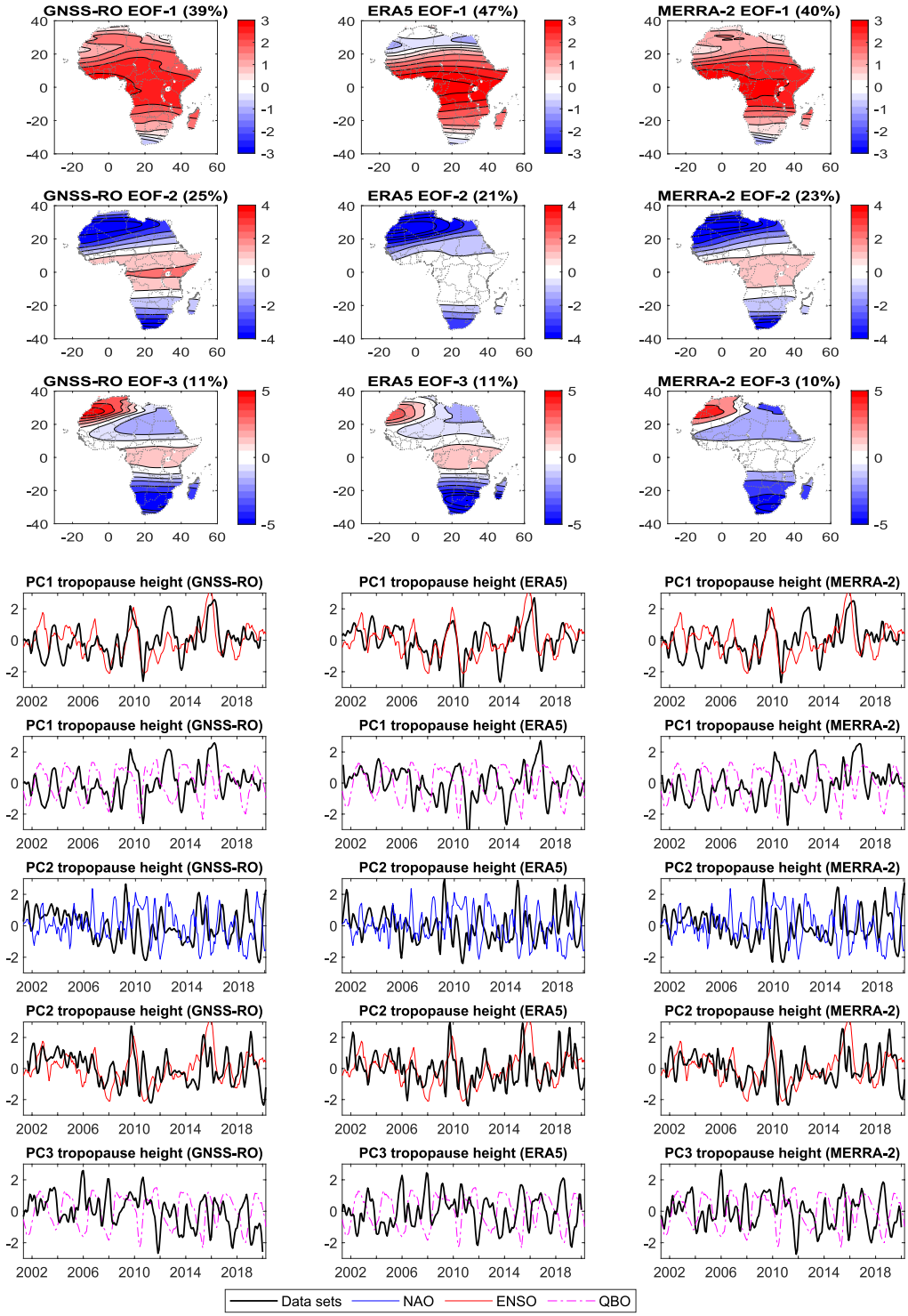

Figure 11. The first three leading empirical orthogonal functions (spatial patterns) of tropopause heights based on Global Navigation Satellite System-Radio Occultation (the first column), European Centre for Medium-Range Weather Forecasts Reanalysis 5 (the second column), Modern-Era Retrospective analysis for Research and Applications version 2 (the third column), and their corresponding principal components (PCs) (lower panels), which are plotted together with some representative global climate drivers' indices that are statistically significant correlated ($p < 0.05$). The PCs are plotted with lag-time to match the climate driver indices. Details for correlation coefficients between each PC and global climate drivers indices are shown in Figure 13.

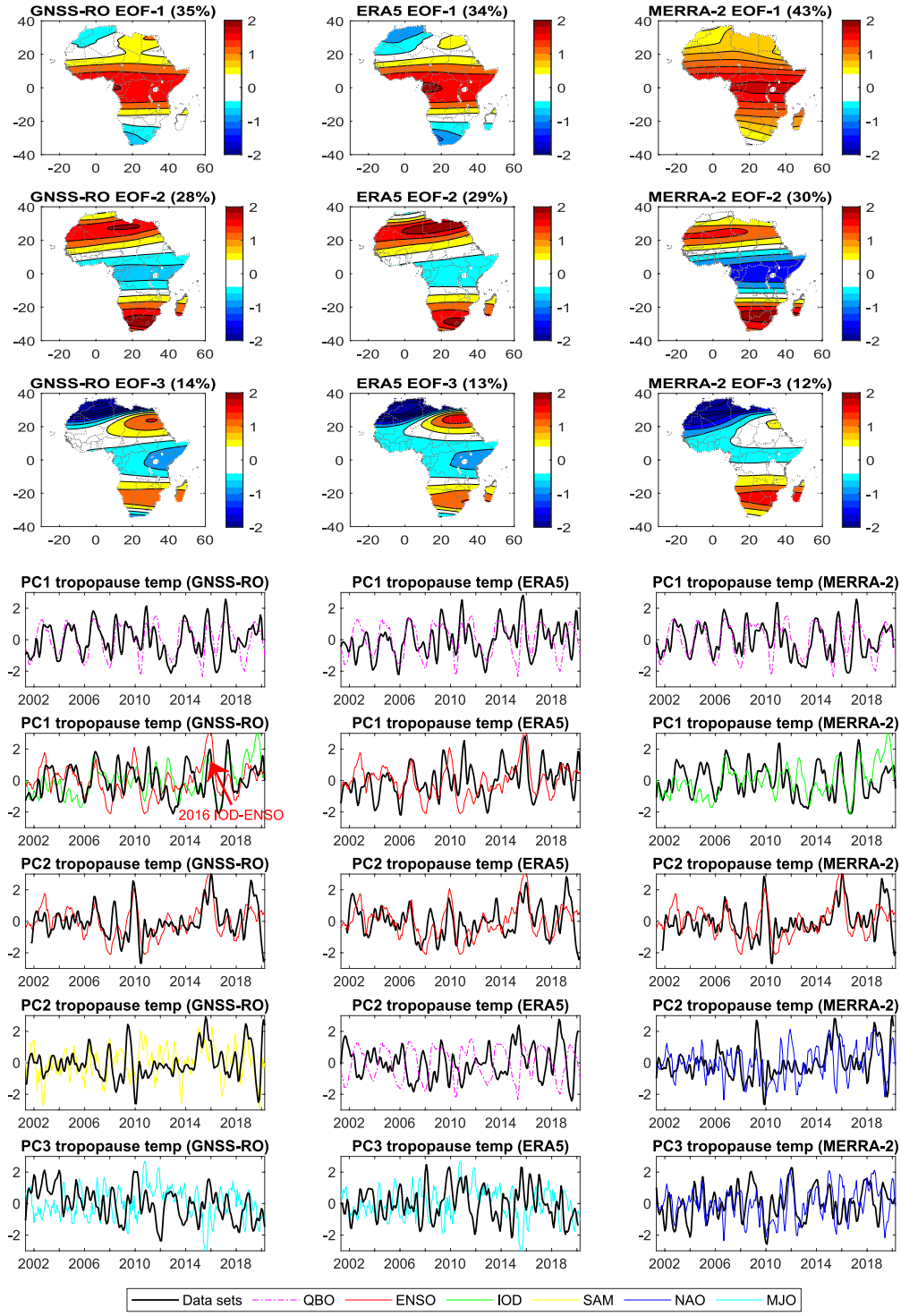

Figure 12. The first three leading empirical orthogonal functions (spatial patterns) of tropopause temperature variability based on Global Navigation Satellite System-Radio Occultation (the first column), European Centre for Medium-Range Weather Forecasts Reanalysis 5 (the second column), Modern-Era Retrospective analysis for Research and Application version 2 (the third column), and their corresponding principal components (PCs) (lower panels), which are plotted together with some representative global climate drivers' indices that are statistically significant correlated ($p < 0.05$). The red arrow indicates coupling of El Niño-Southern Oscillation and Indian Ocean Dipole in 2016–2017. The PCs are plotted with lag-time to match the climate driver indices. Details for correlation coefficients and lag time between each PC and global climate drivers indices are shown in Figure 13.

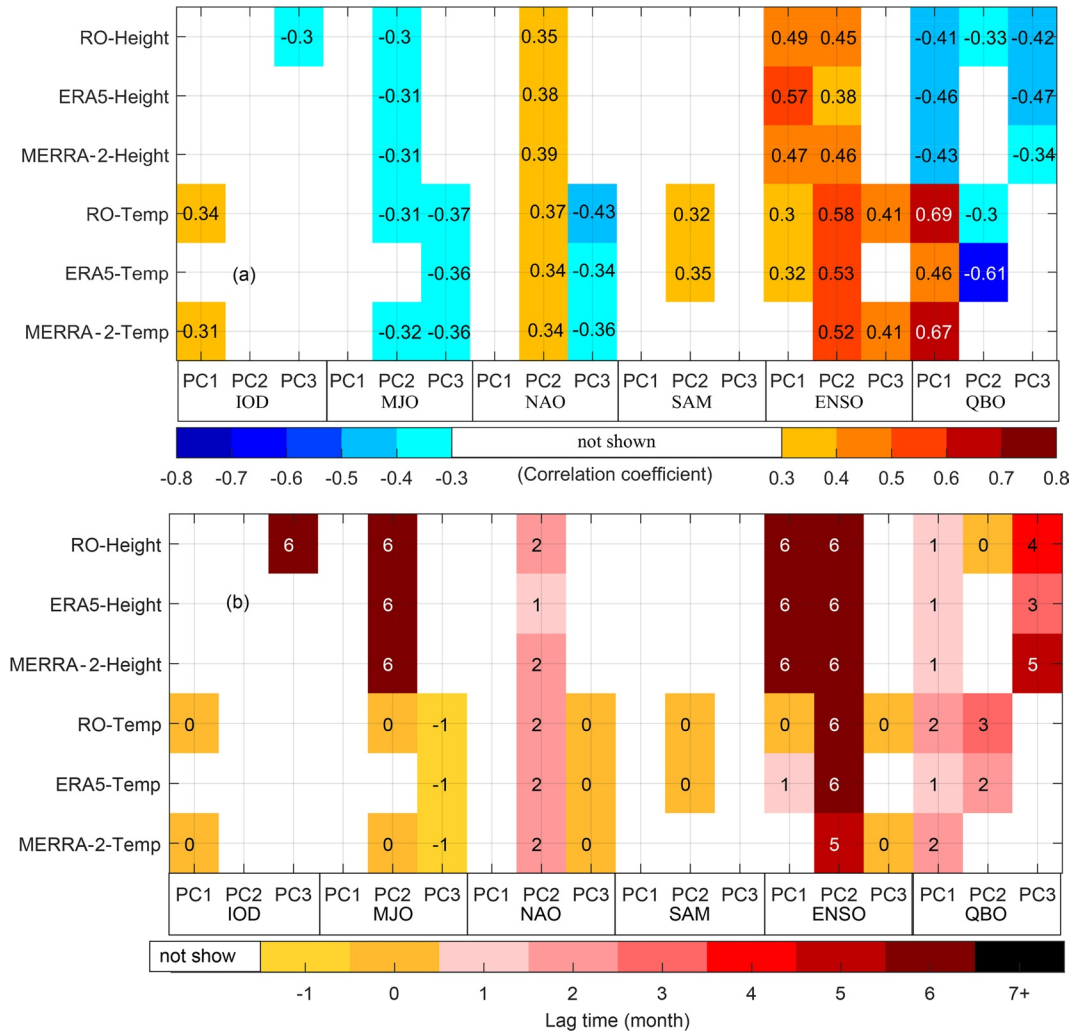

Figure 13. (a) Correlation coefficients between global climate indices and principle component time series of tropopause height and temperature from Global Navigation Satellite System-Radio Occultation and reanalysis products. Only results that are statistically significant and have correlations higher than 0.3 are shown. (b) Lag time (in months) where the maximum correlations are obtained.

correlation coefficients (at a lag of 6 months) are 0.49, 0.57, and 0.47, respectively, for the three data sets, see Figure 13. The product of the EOF1 and the PC1, reveals a higher tropopause height over Africa during El Niño events. The ENSO signal is weaker in tropopause temperature variability. Highest correlation coefficients are found for PC2 with correlations of 0.58 (at a lag of 6 months), 0.53 (6 months), and 0.52 (5 months) for GNSS-RO (28%), ERA5 (29%), and MERRA-2 (30%), respectively, indicating lower tropopause temperature variability over Central and Eastern Africa as being associated with El Niño, see Figure 12. The spatial patterns are symmetric about the equator and reveal lower tropopause temperature variability at equatorial latitudes and higher temperature variability poleward of ∼15°S/N. The difference between the sub-equatorial (0°S/N–10°S/N) and tropical region (15°S/N–35°S/N) is apparently influenced by both La Niña and El Niño. Responses of convection and rainfall patterns to ENSO are however modulated by sea surface temperature anomalies of the adjacent Atlantic and Indian Ocean (Hart et al., 2019; Nicholson & Kim, 1997). The PC2 on the other hand is associated with prolonged tropical Pacific sea surface temperature anomalies (e.g., 2009–2010 (El Niño), 2010–2011 (La Niña), and 2014–2016 (El Niño)).

QBO is another dominant driver of the African tropopause variability. Due to the interaction between ENSO and QBO (Geller et al., 2016), EOF1/PC1 of tropopause height (Figure 11) also contains some QBO signals. The correlations between PC1 and the QBO index amount to −0.41, −0.46, and −0.43, respectively for the three data

sets, and are statistically significant. Maximum correlation is obtained at a lag of 1 month (see Figure 13). A stronger signal is found in tropopause temperature with correlation coefficients (time lags of maximum correlation) between the QBO index and the first PC of tropopause temperature being 0.69 (2 months), 0.46 (1 month), and 0.67 (2 months), for GNSS-RO (35% of variance), ERA5 (34%), and MERRA-2 (43%), respectively. Corresponding EOFs reveal a negative zonally symmetric low-latitude signal. In 2016, both tropopause heights and ENSO were the highest in Africa, and the QBO amplitudes were weaker and had a shorter phase in the ascending period, see Figure 11 (EOF1 and PC1). This could suggest positive tropopause heights anomalies associated with El Niño that decrease and weakens QBO, while negative tropopause height anomalies in Africa in 2011 is related to La Niña, the QBO amplitudes were greater and had slower phase propagation. Taguchi (2010) noticed that QBO exhibited weaker amplitudes and faster phase propagation during El Niño years. A recent study (i.e., Kawatani et al., 2019) explored this mechanism that ENSO modulation of QBO, found that stronger tropical upwelling associated with stratospheric circulation during El Niño, are overcome by enhanced wave driving, leading to the shorter QBO cycles, which confirmed Taguchi (2010).

PC1 of tropopause temperature is also correlated with the ENSO and IOD index (see Figures 12 and 13). Coupling of ENSO and IOD was strong in 2016–2017 (indicated by the red arrow in Figure 12). Lim and Hendon (2017) found that the IOD event was a key promoter of the ENSO event.

MJO shows a moderate impact on African tropopause variability, mainly over northeast and Southern Africa (Figure 10) and is captured by PC2 in both, tropopause height and tropopause temperature, and by PC3 of tropopause temperature with correlation coefficients of −0.37 (Figure 13). Figure 13 suggests complex interplay between NAO, ENSO, and MJO reflected at the tropopause (see EOF2 and PC2 in Figure 11). The coupling of MJO and positive NAO is enhanced (suppressed) via the tropospheric Rossby wave propagation during El Niño (La Niña) due to enhanced wave activity, while the coupling of MJO and negative NAO is enhanced (suppressed) via the lower stratosphere during La Niña (El Niño) dependent on the condition of the stratospheric polar vortex (Lee et al., 2019).

SAM is found in the second PC of tropopause temperature from GNSS-RO and ERA5 (Figure 12), with positive correlation coefficients ranging from 0.3 to 0.4, at lags less than 1 month (Figure 13). NAO is captured in PC2 in tropopause height and temperature, and in PC3 of tropopause temperature, with correlation coefficients between 0.3 and 0.5 at time lags between 0 and 2 months (Figure 13).

There is an overall good agreement between reanalyses and GNSS-RO data on detecting the connection to climate drivers at the tropopause, indicating that the African tropopause is subject to but not limited to the linkage of ENSO, QBO, IOD, NAO, MJO, and SAM. This study shows that modern reanalyses that assimilate Radio Occultation data can also detect these large-scale climate drivers (Tegtmeier et al., 2020). Furthermore, ranking the influence of global climate drivers on tropopause variability by product of the PCs' variances and the magnitude of the correlation values yields (a) ENSO, (b) QBO, (c) NAO, (d) MJO, (e) IOD, and (f) SAM for the tropopause height and (a) QBO, (b) ENSO, (c) IOD, (d) NAO, (e) SAM, and (f) MJO for tropopause temperature.

3.2.2. Variability in Relation to Regional Climate Drivers

We further employ ICA to reveal some of the signals that cannot be detected by the PCA approach, such as the TEJ, ITCZ, WAM, and total ozone in Southern Africa. PCA is a pre-step for constructing ICA. The first five PCs (not shown), which represent more than 90% of the total variance in the tropopause variability, are considered to be sufficient to describe the African tropopause variability. Only interpretable independent components (i.e., the spatial and temporal patterns from ICA that match the behavior of regional climate drivers) are shown in Figures 14 and 15. The rest are provided in Supporting Information S1. The spatial patterns are split into positive and negative parts for better interpretability.

A statistically significant correlation of 0.91 ($p < 0.05$) is observed between the ITCZ and tropopause variability based on GNSS-RO (IC-1), see Figure 14c. The seasonal amplitude of the ITCZ is captured well in the figure. The strong negative signal near northeast Africa (Figure 14b) represents the linkage between the ITCZ and the tropopause height in July, suggesting that the tropopause height and ITCZ have a positive relationship, where rising tropopause altitude near northeast Africa in this month (Figure 14b), was associated with a decrease in the coverage of deep convection (Figure 14a) (Gettelman et al., 2002). This is related to the "upped-ante mechanism" and influenced by Asian summer monsoon through atmospheric teleconnections (Gettelman & Birner, 2007; Neelin et al., 2003). ITCZ is also strongly correlated with the IC-5 derived from GNSS-RO tropopause height

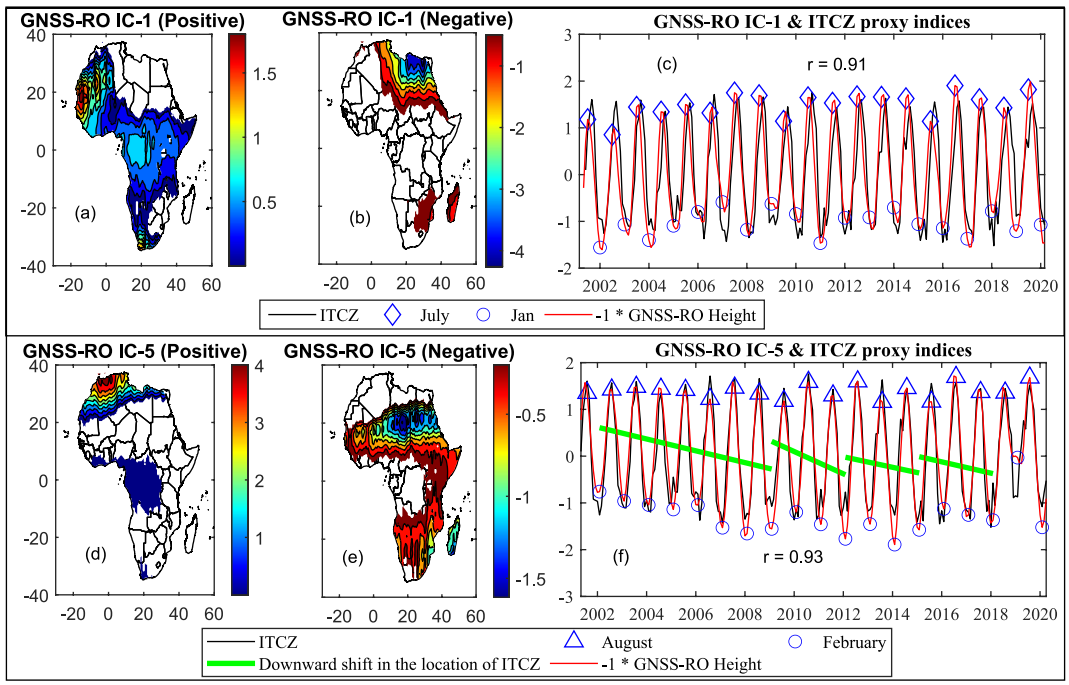

Figure 14. Independent Components derived from Global Navigation Satellite System-Radio Occultation tropopause height fields. Black time-series represent the proxy Intertropical Convergence Zone (ITCZ) index. Each spatial IC pattern is split into positive and negative parts for better interpretability. The spatial pattern and time series were flipped to match regional climate indices. The positive spatial pattern has a positive amplitude and vice versa. Right panels: The correlation coefficients (*r*) between ICs and regional climate proxy indices are provided. The green line in panel (f) indicate the downward shift in the ITCZ's position in relation to El Niño-Southern Oscillation episodes. The correlation coefficients are at 95% confidence level.

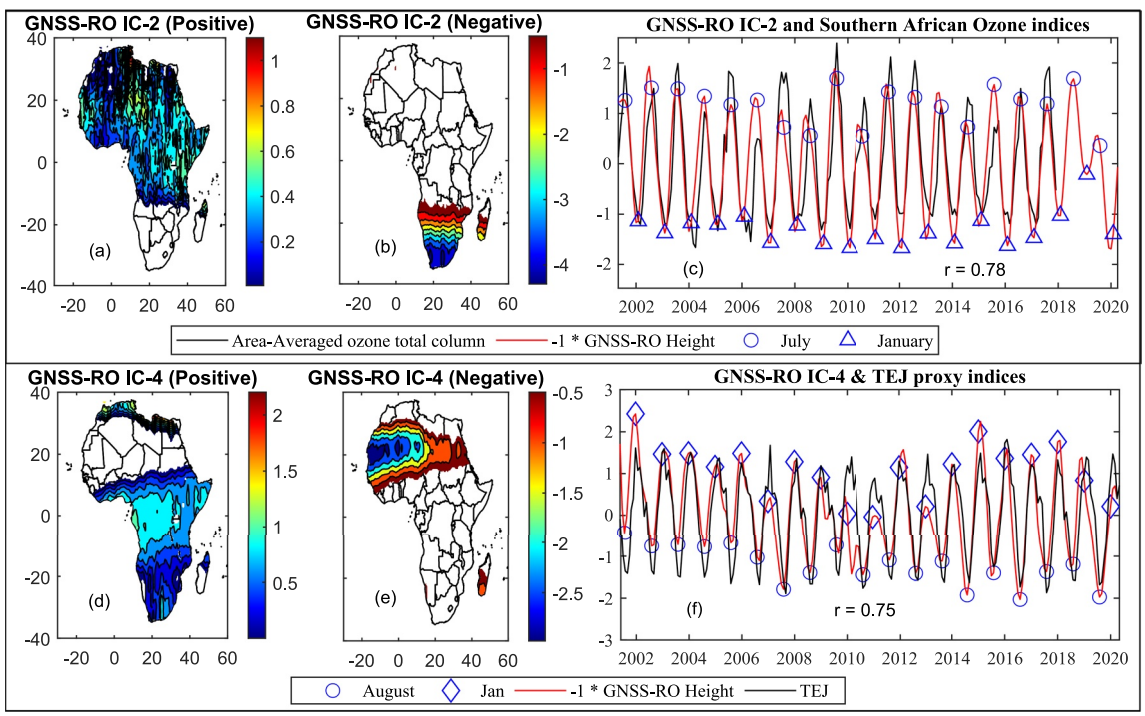

Figure 15. The African independent tropopause height variability patterns derived from independent components analysis of Global Navigation Satellite System-Radio Occultation data and Southern African total ozone column (a–c) and Tropical Easterly Jet (d–f). The spatial patterns and time series were flipped to match regional climate indices.

($r = 0.93$; $p < 0.05$, e.g., Figure 14f). The change in the location of ITCZ (see Figure 14e) coincides with the occurrence of the El Niño event. The time series suggests a possible relationship with strong ENSO events. The downward shift in ITCZ's position from 2002 to 2009, corresponds to a northward shift in ITCZ. In 2009/2010, a strong El Niño shifted ITCZ back to the early 2000 conditions. It then resumed its northward shift from 2013 to 2015 until another major El Niño event happened in late 2015. This signal suggests a rising tropopause height that might be associated with a southward displacement of ITCZ. Pausata et al. (2020) also simulated a similar interactive pattern of ENSO-ITCZ based on a climate model in the UTLS and suggested that Northern Hemisphere (NH) Tambora-like eruption induced hemispheric asymmetric cooling of the upper troposphere shifted the ITCZ toward the equator, leading to an El Niño like response. This signal is consistent with Broccoli et al. (2006), who suggested that the ITCZ tends to approach the warmer hemisphere during the positive ENSO phase.

Figure 15b and 15c shows the relationship between the total ozone column and tropopause height in Southern Africa. In this study, a positive correlation of 0.78 ($p < 0.05$) is observed between the tropopause height and Southern African total ozone from 2001 to 2018. Steinbrecht et al. (1998) found that the tropopause height is negatively correlated with total ozone. Moreover, they suggest an increase in tropopause height contributes significantly to the total ozone depletion. Our results show similar patterns: a high tropopause height is associated with low total ozone and a low tropopause height with high total ozone, but we fail to observe a significant trend in tropopause height due to the short timescale.

Figures 15d–15f reveal that IC4 of tropopause height variability and TEJ have a statistically significant correlation of 0.75 ($p < 0.05$). The results are consistent with those of Nicholson and Klotter (2021), who showed that TEJ sustains a maximum strength at 150 hPa during August over the regions of 10°W–30°E and 5°N–15°N. Moreover, the temporal patterns indicate a relationship between tropopause height and TEJ (Figure 15f). Grist and Nicholson (2001) showed that the tropospheric temperature gradient has linkage with the intensity of TEJ in the latitudinal region higher than 10°N. In addition, other factors appear to control the strength of TEJ, including the contrast of sea surface temperature over the southern subtropical Indian Ocean and central equatorial Pacific, the latitudinal shift of upper-tropospheric easterlies and westerlies in the SH, and cooler tropical upper-tropospheric temperature (Nicholson & Klotter, 2021). This suggests La Niña (i.e., 2010–2011 in Figure 15f) induces global upper-tropospheric cooling (decrease in tropopause height) and is associated with a widespread and sustained TEJ.

The positive and negative spatial patterns and time series representing the annual cycle of WAM is shown in Figures 16a–16c. WAM is highly correlated with IC5 of tropopause temperature variability ($r = 0.72$; $p < 0.05$). Positive increase in the temporal patterns is followed by the evolution of the pre-onset phase (November–March; Figure 16c). A northward migration of the rainy season, which starts in March from approximately 5°N, marks the end of the pre-onset phase corresponding to the positive decrease in the temporal patterns, which is followed by positive spatial patterns. GNSS-RO observes a strong and explicit signal near Sahel Africa (Figure 16b), and it tends to become more assertive from March until it is fully developed in May. This corresponds to increased convective activities related to ITCZ during the onset phase. Subsequently, the spatial signal transitions to the next phase, which is the monsoon jump, as the heavy rain gradually shifts northward and the rainy season begins in the Sahel region (12.5°N–20°N) during July and August. This stage indicates that the monsoon is fully developed, corresponding to the negative decrease in the temporal pattern and the positive part of the spatial pattern (Figure 16a). The negative increase over time and transiting to negative spatial pattern, corresponding to the southward migration, mark the second rainfall season in West Africa. The protruding corner (see the northernmost domain in Figure 16b) possibly reveals a sharpened monsoon jump. An abrupt shift in ITCZ leading to the monsoon jump could be due to an interaction with the topography of the Ahaggar Mountains (Sultan & Janicot, 2003). The negative correlation between WAM and tropopause temperature suggests that it is correlated with a strong WAM. Figures 16d–16f show the influence of ENSO on the migration of WAM ($r = 0.64$; $p < 0.05$). The pattern depicts that during La Niña, the tropopause height is lower than normal in Central Africa and higher than normal in Northern Africa. Thus, a higher atmospheric pressure gradient leads to a stronger TEJ exerts WAM travel to the Sahel region, resulting in increased rainfall. During El Niño, the tropopause height is lower than normal in Northern Africa and higher than normal in Central Africa, and the TEJ is weaker, which suppresses WAM to stay near the coastal side and shifts ITCZ toward the equator, and consequently, rainfall deficit in Sahel Region (see Joly & Voldoire, 2009; Nicholson et al., 2007). Climate models and reanalysis products

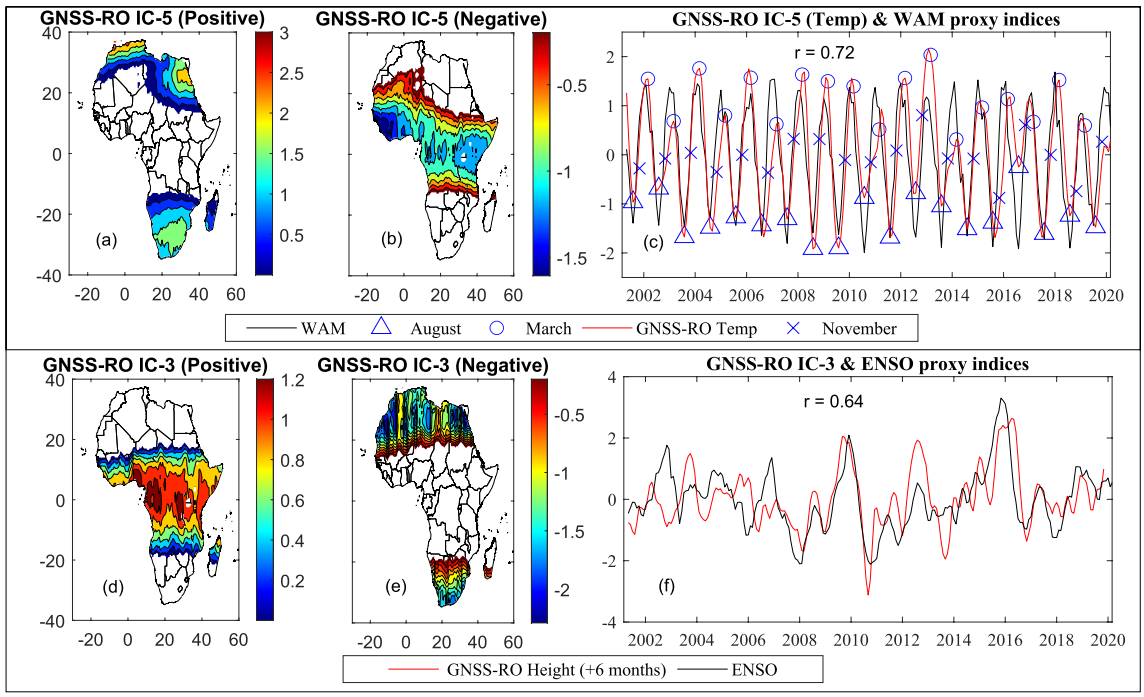

Figure 16. West African Monsoon (WAM; a–c) and El Niño-Southern Oscillation (ENSO; d–f). ENSO signal is derived from tropopause height variability, while WAM is represented by tropopause temperature variability. The correlations are computed at 95% confidence level.

have revealed these interactions between global and regional climate drivers but not yet studied through observational records over Africa. Overall, this study shows GNSS-RO can also observe these signals.

3.2.3. Variability in Relation to Asian Summer Monsoon

Figure 17 shows patterns of the long-term monthly mean tropopause heights based on GNSS-RO observations, which are also revealed from tropopause temperature. The sub-plot in July shows a relationship between tropopause in northeast Africa and Asian summer monsoon. In JJA, tropopause heights tend to be highest in the northeastern part of the domain, which is possibly attributed to the tropopause structure over the Middle East and the Tibetan Plateau to the Asian summer monsoon convective heating (Highwood & Hoskins, 1998). For instance, the tropopause height in July reveals an asymmetric tropical tropopause height between the East African coast and the Iranian Plateau-Arabian Sea being highest over the Northeast African coast and lowest over the West Indian Ocean. Such a unique pattern is also observed from MERRA-2 and ERA5 and consistently occurs during June–August (most pronounced in July) and corresponds to the interannual variation of Asian summer monsoon (Highwood & Hoskins, 1998; Randel & Park, 2006). Tropopauses in other seasons and regions reveal smaller differences between the two regions. In addition, the tropopause height tends to show little north-south gradient across the continent in other months and seasons, but tends to be more uniformly distributed, unlike the pattern in June–August, when it is skewed to the Northeast African coast. This pattern could be attributed to two drivers. First, June–August period coincides with the peak of the Asian Summer Monsoon Anticyclone within the UTLS. This tends to influence horizontal mass distribution stretching from the West African coast to the Pacific (as also demonstrated in Basha et al., 2021). Second, during the northern summer, the Asian monsoon interacts with the TEJ, with TEJ potentially inducing additional circulation and convection over south Asia (due to warming over East Indian Ocean), while suppressing vertical flow over equatorial Africa (due to cooling over West Indian Ocean), see for example, Pan et al. (2016).

3.2.4. Discussion

Over a continental scale, ENSO and QBO have the most significant impact on the African tropopause variability, but their influence on different regions varies significantly. Starting in May, the wet and warm air developed by El Niño is transported to East Africa, reaching the east side of the Rift in September-October, when the core of TEJ begins to approach the equator. The air encounters orographic gravitational-wave induced by the East African

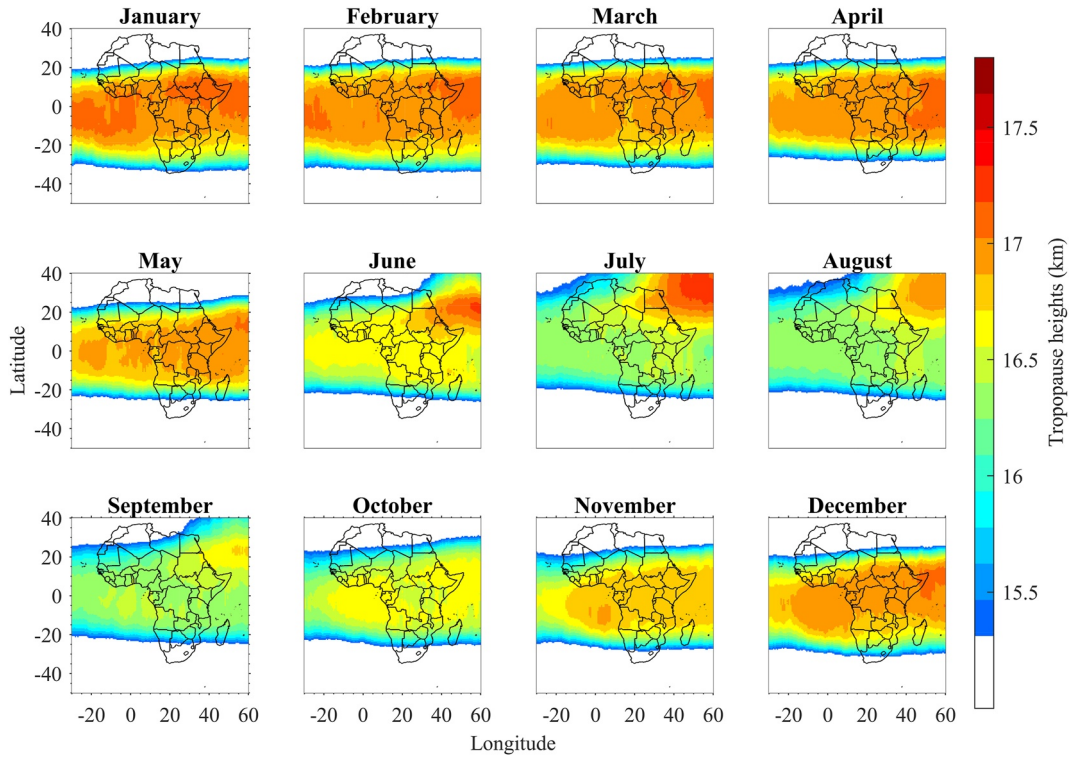

Figure 17. Monthly long-term means for tropopause heights (January–December) based on Global Navigation Satellite System-Radio Occultation observations.

highlands (McFarlane, 1987). The moisture content modifies the associated lapse rate due to gravitational waves, providing an uplift to allow additional condensation (Lamarque et al., 1996). Tropopause temperatures have been shown to control the amount and distribution of lower stratospheric water vapor, which in turn influences chemistry, radiation, and circulation in the stratosphere, and can also be an important driver of surface climate, with the 2-year and 5-year peaks of tropopause temperature strongly linked to QBO and ENSO, respectively (Wang et al., 2016). QBO and ENSO are strongly linked to interannual variability of climate in different regions in Africa. As indicated in Lu et al. (2020), tropical tropopause temperature is the main factor controlling lower stratospheric water vapor, and hence regulation of global radiation budget, energy balance and thus global warming. ENSO can also influence tropical upwelling and tropopause temperature as it is one of the most important processes controlling UTLS water vapor changes on interannual time scale.

Perhaps another interesting feature in East Africa is active volcanoes. Vast amounts of ash and aerosols are transported to the lowermost stratosphere and consequently influence the ENSO teleconnection signal of tropopause temperature. The TEJ and atmospheric circulations require a large amount of water supply and consequently regular tropical upwelling (see Schott et al., 2009), which influences sub-seasonal tropical lowermost stratosphere temperature (Abalos et al., 2012). During positive IOD, which tends to occur with El Niño, a low-pressure system forms near East Africa, and a high-pressure system forms in the East Indian Ocean, amplifying the easterly wind stress, thereby more upwelling in the East Indian Ocean, and Walker circulation transports moisture to East Africa (Hirons & Turner, 2018).

Over Northern Africa, the ENSO and NAO were observed to influence the tropopause properties that are associated with climate and weather systems. The influence of NAO is most predominant in boreal winter when the westerly locates further south. NAO displays an impact on the transfer of moisture and heat in northwest Africa (Hurrell et al., 2003), but reduces the influence of regional-scale atmospheric circulation further inland. It can be explained by the diverged transient momentum flux associated with a damped westerly jet over Northern Africa (Lin et al., 2009). The climate of this region is highly dependent on nearby areas such as Western Africa.

A very complex regional climate system is seen in Western and Central Africa. In boreal summer, the TEJ and ITCZ lie across the Sahel region, when the WAM is most developed. Intraseasonal variability is associated with MJO constant propagation through the region. The core of deep convective activities is around 10°N. As the El Niño arrives, the teleconnection signal shows two hotspots of tropopause temperature increase near the west coast (5°N–15°N and 5°S–15°S). MJO seems to serve as the pathway of the teleconnection of ENSO (see Figures 10D1–10F1 and 10D2–10F2). The influence of ENSO is linked to the late-onset WAM and the rainy season. The increased horizontal hydrostatic pressure gradient during El Niño leads to fast eastward moving MJO episodes (see Section 3.2.1 and Zeng et al., 2012), associated with reduced convection over West Africa. This is explained by Neelin et al. (2003) that warmer tropospheric temperatures increase surface boundary layer moisture required for convection to occur, also known for "upped-ante mechanism." Also, ENSO causes diagonal displacement of meridional atmospheric pressure gradient, which influences subsidence over the central landmass (see Figures 10D1–10F1), which in turn shifts wind and moisture gradient. Moreover, the ENSO-induced atmospheric pressure change over this region is directly associated with NAO development (Hurrell et al., 2003). These changes in this region reduce the monsoon momentum and push NH ITCZ southward. A weakened WAM could be expected during El Niño (Giannini et al., 2007). However, the arrival of MJO may fuel the longevity and momentum of WAM (Lavender & Matthews, 2009). The arrival of MJO has significant influence to the climate and weather of tropical Africa. In boreal winter, a negative NAO can mitigate the impact of El Niño in western Africa. A low-pressure system near the western African coast activates local circulations and brings moist air inland, in conjunction with El Niño pushing the SH ITCZ equatorward (McHugh & Rogers, 2001), and consequently triggers drought conditions in Southern Africa as the SH ITCZ moved away.

Over Southern Africa, the climate and weather patterns are associated with SAM and ENSO. ENSO usually reaches Southern Africa in boreal winter. In El Niño, the tropical tropopause height increases distinctly, and the coverage by deep convection decreases exponentially (Gettelman et al., 2002). Moreover, increased upper-tropospheric temperature interacts with dry air from the Kalahari Desert. It requires higher moisture content to form convection, leading to reduced precipitation over South Africa and neighboring countries due to tropospheric warming at tropical latitudes and reduced pressure gradient force that affect wind patterns. Thus, drought conditions are usually expected in Southern Africa during El Niño (Nicholson, 2011). On the other hand, La Niña has the opposite effect. The geopotential height field in tropical tropopause decreases, higher pressure in Central Africa forces SH ITCZ to move southward, and Southern Africa expects increased rainfall. As such, frequent sea breeze effects emerge and further induce upwelling activities near Southern Africa. The negative/positive SAM (i.e., northward/southward westerly) are associated with enhanced/reduced rainfall in Southern Africa in El Niño/La Niña (Silvestri & Vera, 2009), due to Ekman flow induced by wind-driven circulation (Ummenhofer & England, 2007).

4. Conclusions

This study addressed the radiosonde data gaps in Africa and demonstrated that it can be infilled using GNSS-RO data from various missions, including CHAMP, GRACE, COSMIC, COSMIC-2, and MetOp-A for the time period of 2001–2020. Altogether, GNSS-RO provides more than 1.5 million accurate, consistent, high-vertical resolution atmospheric profiles over the African continent, which has typically had deficient, inconsistent, or poor-quality upper-air measurements. Over recent decades, the African radiosonde network has been shrinking at an estimated rate of 50 stations/decade and 300,000 observations/decade. Today, only 50 stations remain active. Overall, 50% of the African radiosonde data are useable, while the rest are either problematic or missing. A statistical comparison and validation between radiosonde measurements and data from various GNSS-RO missions revealed good agreement with differences being smaller than 1 K across the UTLS region (10–25 km). Furthermore, this study revealed potential issues with using reanalysis products to infill the radiosonde gap over Africa, that is, (a) they are rather smooth profiles with only little vertical variability, limiting their ability to detect tropopause inversion layers, (b) they sometimes underestimate the seasonal variations and suffer from temporal inhomogeneity of tropopause heights, and (c) tropopause temperatures/heights of ERA5 and MERRA-2 are biased at low latitudes by 0.8 K/0.3 km and 1.2 K/0.5 km, respectively. Statistical comparisons between radiosondes, GNSS-RO, and reanalysis products demonstrated best agreement between radiosonde measurements and GNSS-RO, having the lowest RMSE and the highest KGE values. GNSS-RO's data availability only began in the

early 2000s, limiting its use for long-term climate applications. Nevertheless, this study showed that GNSS-RO outperformed reanalysis products in addressing the radiosonde data gaps over Africa.

The analysis of GNSS-RO data also revealed a better understanding of tropopause variability over Africa for the period 2001–2020 in relation to global and regional climate drivers. The following results were obtained:

1. Statistically significant signals of ENSO, QBO, NAO, MJO, IOD, and SAM were found in deseasonalized time series of tropopause temperatures and heights based on correlation analysis as well as PCA. Annual variability of teleconnection of ENSO, QBO, NAO, MJO, IOD, and SAM are seen across different regions over Africa, with ENSO being strong in tropopause heights while QBO being strong in tropopause temperature. Several coupled global climate drivers, for example, ENSO-IOD, ENSO-QBO, ENSO-NAO, QBO-IOD, ENSO-MJO, and ENSO-SAM-MJO were also observed.
2. Statistically significant signals of ITCZ, TEJ, WAM, and ozone variation in Southern Africa were detected using ICA. GNSS-RO observations suggest that the tropopause height increases and temperature decreases due to global natural variability associated with El Niño events, which cause hemispheric asymmetry in the upper tropospheric temperature in the tropics that cause the ITCZ to move southward.
3. The relationship between local air-sea interaction and tropopause variability has been studied. During July, the Asian summer monsoon affects the zonal symmetry behavior and mean latitudinal gradients of the tropical tropopause in Africa.

This study has therefore pioneered the use of GNSS-RO to investigate the African atmospheric variability. Future studies will investigate the complex interaction of various climate drivers and their roles in the changing climate. While many climate drivers have shown their footprint in the tropopause layer, their contributions and interactive mechanisms to atmospheric climate change are still not well understood in this study. Reanalyses assemble various data sets, which to some extent, compromise their accuracies due to data fusion. By contrast, the GNSS-RO relies on a single data source, making it a powerful tool for studying atmospheric climate change behavior. With more publicly available data from various satellites, GNSS-RO may, in future, play a significant role in monitoring atmospheric climate change and regional climate forecasts. In particular for Africa, GNSS-RO will be a primary data source for many countries.

Data Availability Statement

All GNSS-RO data used during this study are openly available from the COSMIC Data Analysis and Archive Center at https://data.cosmic.ucar.edu/gnss-ro/champ/repro2016/ (CHAMP; CDAAC GNSS Radio Occultation Datasets, 2001), https://data.cosmic.ucar.edu/gnss-ro/grace/postProc/ (GRACE; CDAAC GNSS Radio Occultation Datasets, 2007), https://data.cosmic.ucar.edu/gnss-ro/metopa/postProc/ (MetOp-A; CDAAC GNSS Radio Occultation Datasets, 2016), https://www.cosmic.ucar.edu/what-we-do/cosmic-1/data (COSMIC; UCAR COSMIC Program, 2006), and https://www.cosmic.ucar.edu/what-we-do/cosmic-2/data (COSMIC-2; UCAR COSMIC Program, 2019). All MERRA-2 data are available at https://doi.org/10.5067/WWQSXQ8IVFW8 (GMAO, 2015). All ERA5 data are available at https://apps.ecmwf.int/data-catalogues/era5/?class=ea (Copernicus Climate Change Service, 2019; Hersbach et al., 2020). All radiosonde station information provided by WMO are available at https://www.wmo.int/. All radiosonde data are openly available at https://doi.org/10.7289/V5X63K0Q (Durre et al., 2016).

Acknowledgments
The authors would like to thank NOAA for providing Integrated Global Radiosonde Archive (IGRA) data. Thanks also to NOAA, GFZ Potsdam, US Air Force (USAF), NSPO, and UCAR for making available the CHAMNP, COSMIC, GRACE, COSMIC and COSMIC-2 data. The authors appreciate Global Modeling and Assimilation Office (GMAO) and ECMWF for providing MERRA-2 and ERA5 data. The authors greatly appreciate the thoughtful comments and suggestions of the three anonymous reviewers. Open access publishing facilitated by Curtin University, as part of the Wiley - Curtin University agreement via the Council of Australian University Librarians.

References

Abalos, M., Randel, W., & Serrano, E. (2012). Variability in upwelling across the tropical tropopause and correlations with tracers in the lower stratosphere. *Atmospheric Chemistry and Physics*, *12*(23), 11505–11517. https://doi.org/10.5194/acp-12-11505-2012

Agutu, N., Awange, J., Zerihun, A., Ndehedehe, C., Kuhn, M., & Fukuda, Y. (2017). Assessing multi-satellite remote sensing, reanalysis, and land surface models' products in characterizing agricultural drought in East Africa. *Remote Sensing of Environment*, *194*, 287–302. https://doi.org/10.1016/j.rse.2017.03.041

Andersson, J. C., Arheimer, B., Traoré, F., Gustafsson, D., & Ali, A. (2017). Process refinements improve a hydrological model concept applied to the Niger River basin. *Hydrological Processes*, *31*(25), 4540–4554. https://doi.org/10.1002/hyp.11376

Angerer, B., Ladstädter, F., Scherllin-Pirscher, B., Schwärz, M., Steiner, A. K., Foelsche, U., & Kirchengast, G. (2017). Quality aspects of the Wegener Center multi-satellite GPS radio occultation record OPSv5. 6. *Atmospheric Measurement Techniques*, *10*(12), 4845–4863. https://doi.org/10.5194/amt-10-4845-2017

Anthes, R. A., Bernhardt, P., Chen, Y., Cucurull, L., Dymond, K., Ector, D., et al. (2008). The COSMIC/FORMOSAT-3 mission: Early results. *Bulletin of the American Meteorological Society*, *89*(3), 313–334. https://doi.org/10.1175/BAMS-89-3-313

Anthes, R. A., & Schreiner, W. S. (2019). Six new satellites watch the atmosphere over Earth's equator. *Eos*, *100*. https://doi.org/10.1029/2019EO131779

Anyah, R., Forootan, E., Awange, J., & Khaki, M. (2018). Understanding linkages between global climate indices and terrestrial water storage changes over Africa using GRACE products. *Science of the Total Environment*, *635*, 1405–1416. https://doi.org/10.1016/j.scitotenv.2018.04.159

Awange, J. (2012). *Environmental monitoring using GNSS: Global navigation satellite systems* (p. 382). Springer-Verlag, Berlin, Heidelber.

Awange, J. (2018). *GNSS environmental sensing*. Springer International Publishers AG.

Awange, J. (2021a). *Lake Victoria monitored from space*. Springer.

Awange, J. (2021b). *Nile waters. Weighed from space*. Springer International Publishers AG.

Awange, J. (2022). *Food insecurity & hydroclimate in greater horn of Africa: Potential for agriculture amidst extremes*. Springer International Publishers.

Awange, J., Anyah, R., Agola, N., Forootan, E., & Omondi, P. (2013). Potential impacts of climate and environmental change on the stored water of Lake Victoria Basin and economic implications. *Water Resources Research*, *49*(12), 8160–8173. https://doi.org/10.1002/2013WR014350

Awange, J., Ferreira, V. G., Forootan, E., Andam-Akorful, S., Agutu, N. O., & He, X. (2016). Uncertainties in remotely sensed precipitation data over Africa. *International Journal of Climatology*, *36*(1), 303–323. https://doi.org/10.1002/joc.4346

Baldwin, M., Gray, L., Dunkerton, T., Hamilton, K., Haynes, P., Randel, W., et al. (2001). The quasi-biennial oscillation. *Reviews of Geophysics*, *39*(2), 179–229. https://doi.org/10.1029/1999RG000073

Basha, G., Kishore, P., Ratnam, M. V., Ouarda, T. B., Velicogna, I., & Sutterley, T. (2015). Vertical and latitudinal variation of the Inter-tropical Convergence Zone derived using GPS radio occultation measurements. *Remote Sensing of Environment*, *163*, 262–269. https://doi.org/10.1016/j.rse.2015.03.024

Basha, G., Ratnam, M. V., Jiang, J. H., Kishore, P., & Ravindra Babu, S. (2021). Influence of Indian summer monsoon on tropopause, trace gases and aerosols in Asian summer monsoon anticyclone observed by COSMIC, MLS and CALIPSO. *Remote Sensing*, *13*(17), 3486. https://doi.org/10.3390/rs13173486

Broccoli, A. J., Dahl, K. A., & Stouffer, R. J. (2006). Response of the ITCZ to northern hemisphere cooling. *Geophysical Research Letters*, *33*(1), L01702. https://doi.org/10.1029/2005GL024546

CDAAC GNSS Radio Occultation Datasets. (2001). CHAMP data products [Dataset]. UCAR/NCAR - COSMIC. Retrieved from https://doi.org/10.5065/qan9-we09

CDAAC GNSS Radio Occultation Datasets. (2007). GRACE data products [Dataset]. UCAR/NCAR - COSMIC. Retrieved from https://doi.org/10.5065/chk8-fx07

CDAAC GNSS Radio Occultation Datasets. (2016). MetOp-A data products [Dataset]. UCAR/NCAR - COSMIC. Retrieved from https://doi.org/10.5065/789w-m137

Chen, G., Iwasaki, T., Qin, H., & Sha, W. (2014). Evaluation of the warm-season diurnal variability over East Asia in recent reanalyses JRA-55, ERA-Interim, NCEP CFSR, and NASA MERRA. *Journal of Climate*, *27*(14), 5517–5537. https://doi.org/10.1175/JCLI-D-14-00005.1

Comon, P. (1994). Independent component analysis, a new concept? *Signal Processing*, *36*(3), 287–314. https://doi.org/10.1016/0165-1684(94)90029-9

Copernicus Climate Change Service. (2018). Ozone monthly gridded data from 1970 to present derived from satellite observations [Dataset]. ECMWF. Retrieved from https://cds.climate.copernicus.eu/cdsapp%23%21/dataset/10.24381/cds.4ebfe4eb%3Ftab%3Doverview

Copernicus Climate Change Service. (2019). ERA5: Fifth generation of ECMWF atmospheric reanalyses of the global climate [Dataset]. Meteorological Archival and Retrieval System (MARS): Copernicus Climate Change Service Climate Data Store (CDS). Retrieved from https://cds.climate.copernicus.eu/cdsapp%23%21/home

D'Errico, J. (2004). Inpaint nans [Software]. MATLAB Central File Exchange. Retrieved from https://www.mathworks.com/matlabcentral/fileexchange/4551-inpaint_nans

Dirksen, R., Sommer, M., Immler, F., Hurst, D., Kivi, R., & Vömel, H. (2014). Reference quality upper-air measurements: GRUAN data processing for the Vaisala RS92 radiosonde. *Atmospheric Measurement Techniques*, *7*(12), 4463–4490. https://doi.org/10.5194/amt-7-4463-2014

Durre, I., Vose, R. S., & Wuertz, D. B. (2006). Overview of the integrated global radiosonde archive. *Journal of Climate*, *19*(1), 53–68. https://doi.org/10.1175/JCLI3594.1

Durre, I., Xungang, Y., Vose, R. S., Applequist, S., & Arnfield, J. (2016). Integrated global radiosonde archive (IGRA) Version 2 [Dataset]. NOAA National Centers for Environmental Information, *10*, V5X63X0Q. Retrieved from https://www.ncei.noaa.gov/access/metadata/landing-page/bin/iso?id=gov.noaa.ncdc:C00975

Durre, I., Yin, X., Vose, R. S., Applequist, S., & Arnfield, J. (2018). Enhancing the data coverage in the integrated global radiosonde archive. *Journal of Atmospheric and Oceanic Technology*, *35*(9), 1753–1770. https://doi.org/10.1175/JTECH-D-17-0223.1

Feng, S., Fu, Y., & Xiao, Q. (2012). Trends in the global tropopause thickness revealed by radiosondes. *Geophysical Research Letters*, *39*(20), L20706. https://doi.org/10.1029/2012GL053460

Fink, A. H., Agustí-Panareda, A., Parker, D. J., Lafore, J.-P., Ngamini, J.-B., Afiesimama, E., et al. (2011). Operational meteorology in West Africa: Observational networks, weather analysis and forecasting. *Atmospheric Science Letters*, *12*(1), 135–141. https://doi.org/10.1002/asl.324

Foelsche, U., Borsche, M., Steiner, A. K., Gobiet, A., Scherllin-Pirscher, B., Kirchengast, G., et al. (2008). Observing upper troposphere–lower stratosphere climate with radio occultation data from the CHAMP satellite. *Climate Dynamics*, *31*(1), 49–65. https://doi.org/10.1007/s00382-007-0337-7

Foelsche, U., Scherllin-Pirscher, B., Borsche, M., Kirchengast, G., & Wickert, J. (2009). Assessing the climate monitoring utility of radio occultation data: From CHAMP to FORMOSAT-3/COSMIC. *Terrestrial, Atmospheric and Oceanic Sciences*, *20*(1), 155. https://doi.org/10.3319/TAO.2008.01.14.01(F3C)

Foelsche, U., Scherllin-Pirscher, B., Ladstädter, F., Steiner, A. K., & Kirchengast, G. (2011). Refractivity and temperature climate records from multiple radio occultation satellites consistent within 0.05. *Atmospheric Measurement Techniques*, *4*(9), 2007–2018. https://doi.org/10.5194/amt-4-2007-2011

Fogt, R. L., & Bromwich, D. H. (2006). Decadal variability of the ENSO teleconnection to the high-latitude South Pacific governed by coupling with the southern annular mode. *Journal of Climate*, *19*(6), 979–997. https://doi.org/10.1175/JCLI3671.1

Fogt, R. L., Bromwich, D. H., & Hines, K. M. (2011). Understanding the SAM influence on the South Pacific ENSO teleconnection. *Climate Dynamics*, *36*(7), 1555–1576. https://doi.org/10.1007/s00382-010-0905-0

Forootan, E., Awange, J., Kusche, J., Heck, B., & Eicker, A. (2012). Independent patterns of water mass anomalies over Australia from satellite data and models. *Remote Sensing of Environment*, *124*, 427–443. https://doi.org/10.1016/j.rse.2012.05.023

Forootan, E., Rietbroek, R., Kusche, J., Sharifi, M. A., Awange, J., Schmidt, M., et al. (2014). Separation of large scale water storage patterns over Iran using GRACE, altimetry and hydrological data. *Remote Sensing of Environment*, *140*, 580–595. https://doi.org/10.1016/j.rse.2013.09.025

Franzke, C. L., Barbosa, S., Blender, R., Fredriksen, H.-B., Laepple, T., Lambert, F., et al. (2020). The structure of climate variability across scales. *Reviews of Geophysics*, *58*(2), e2019RG000657. https://doi.org/10.1029/2019RG000657
Fujiwara, M., Hibino, T., Mehta, S. K., Gray, L., Mitchell, D., & Anstey, J. (2015). Global temperature response to the major volcanic eruptions in multiple reanalysis data sets. *Atmospheric Chemistry and Physics*, *15*(23), 13507–13518. https://doi.org/10.5194/acp-15-13507-2015
Gelaro, R., McCarty, W., Suárez, M. J., Todling, R., Molod, A., Takacs, L., et al. (2017). The Modern-Era retrospective analysis for research and applications, version 2 (MERRA-2). *Journal of Climate*, *30*(14), 5419–5454. https://doi.org/10.1175/JCLI-D-16-0758.1
Geller, M. A., Zhou, T., & Yuan, W. (2016). The QBO, gravity waves forced by tropical convection. *Journal of Geophysical Research: Atmospheres*, *121*(15), 8886–8895. https://doi.org/10.1002/2015JD024125
Gettelman, A., & Birner, T. (2007). Insights into tropical tropopause layer processes using global models. *Journal of Geophysical Research*, *112*(D23), D23104. https://doi.org/10.1029/2007JD008945
Gettelman, A., Salby, M., & Sassi, F. (2002). Distribution and influence of convection in the tropical tropopause region. *Journal of Geophysical Research*, *107*(D10), ACL6-1–ACL6-12. https://doi.org/10.1029/2001JD001048
Giannini, A., Robertson, A. W., & Qian, J.-H. (2007). A role for tropical tropospheric temperature adjustment to El Niño-Southern Oscillation in the seasonality of monsoonal Indonesia precipitation predictability. *Journal of Geophysical Research*, *112*(D16), D16110. https://doi.org/10.1029/2007JD008519
GMAO. (2015). 3-Hourly, instantaneous, model-level, assimilation, assimilated meteorological fields V5.12.4-MERRA-2inst3_3d_asm_Nv: 3d [Dataset]. Goddard Earth Sciences Data and Information Services Center (GES DISC). Retrieved from https://gmao.gsfc.nasa.gov/reanalysis/MERRA-2/data_access/
Gregory, P. J., Ingram, J. S., & Brklacich, M. (2005). Climate change and food security. *Philosophical Transactions of the Royal Society B: Biological Sciences*, *360*(1463), 2139–2148. https://doi.org/10.1098/rstb.2005.1745
Grist, J. P., & Nicholson, S. E. (2001). A study of the dynamic factors influencing the rainfall variability in the West African Sahel. *Journal of Climate*, *14*(7), 1337–1359. https://doi.org/10.1175/1520-0442(2001)014<1337:ASOTDF>2.0.CO;2
Gupta, H. V., Kling, H., Yilmaz, K. K., & Martinez, G. F. (2009). Decomposition of the mean squared error and NSE performance criteria: Implications for improving hydrological modelling. *Journal of Hydrology*, *377*(1–2), 80–91. https://doi.org/10.1016/j.jhydrol.2009.08.003
Hansen, J., Sato, M., Glascoe, J., & Ruedy, R. (1998). A common-sense climate index: Is climate changing noticeably? *Proceedings of the National Academy of Sciences of the United States of America*, *95*(8), 4113–4120. https://doi.org/10.1073/pnas.95.8.4113
Hart, N. C., Washington, R., & Maidment, R. I. (2019). Deep convection over Africa: Annual cycle, ENSO, and trends in the hotspots. *Journal of Climate*, *32*(24), 8791–8811. https://doi.org/10.1175/JCLI-D-19-0274.1
Hersbach, H., Bell, B., Berrisford, P., Hirahara, S., Horányi, A., Muñoz-Sabater, J., et al. (2020). The ERA5 global reanalysis. *Quarterly Journal of the Royal Meteorological Society*, *146*(730), 1999–2049. https://doi.org/10.1002/qj.3803
Highwood, E., & Hoskins, B. (1998). The tropical tropopause. *Quarterly Journal of the Royal Meteorological Society*, *124*(549), 1579–1604. https://doi.org/10.1002/qj.49712454911
Hirons, L., & Turner, A. (2018). The impact of Indian Ocean mean-state biases in climate models on the representation of the east African short rains. *Journal of Climate*, *31*(16), 6611–6631. https://doi.org/10.1175/JCLI-D-17-0804.1
Ho, S.-P., Anthes, R. A., Ao, C. O., Healy, S., Horanyi, A., Hunt, D., et al. (2020). The COSMIC/FORMOSAT-3 radio occultation mission after 12 years: Accomplishments, remaining challenges, and potential impacts of COSMIC-2. *Bulletin of the American Meteorological Society*, *101*(7), E1107–E1136. https://doi.org/10.1175/BAMS-D-18-0290.1
Ho, S.-P., Kirchengast, G., Leroy, S., Wickert, J., Mannucci, A. J., Steiner, A., et al. (2009). Estimating the uncertainty of using GPS radio occultation data for climate monitoring: Intercomparison of CHAMP refractivity climate records from 2002 to 2006 from different data centers. *Journal of Geophysical Research*, *114*(D23), D23107. https://doi.org/10.1029/2009JD011969
Ho, S.-P., Peng, L., & Vömel, H. (2017). Characterization of the long-term radiosonde temperature biases in the upper troposphere and lower stratosphere using COSMIC and MetOp-A/GRAS data from 2006 to 2014. *Atmospheric Chemistry and Physics*, *17*(7), 4493–4511. https://doi.org/10.5194/acp-17-4493-2017
Homeyer, C. R., Bowman, K. P., & Pan, L. L. (2010). Extratropical tropopause transition layer characteristics from high-resolution sounding data. *Journal of Geophysical Research*, *115*(D13), D13108. https://doi.org/10.1029/2009JD013664
Hsu, K.-L., Gao, X., Sorooshian, S., & Gupta, H. V. (1997). Precipitation estimation from remotely sensed information using artificial neural networks. *Journal of Applied Meteorology*, *36*(9), 1176–1190. https://doi.org/10.1175/1520-0450(1997)036<1176:PEFRSI>2.0.CO;2
Hurrell, J. W., Kushnir, Y., Ottersen, G., & Visbeck, M. (2003). An overview of the North Atlantic Oscillation. *Geophysical Monograph-American Geophysical Union*, *134*, 1–36. https://doi.org/10.1029/134GM01
Hyvärinen, A., & Oja, E. (2000). Independent component analysis: Algorithms and applications. *Neural Networks*, *13*(4–5), 411–430. https://doi.org/10.1016/S0893-6080(00)00026-5
Inai, Y., Shiotani, M., Fujiwara, M., Hasebe, F., & Vömel, H. (2015). Altitude misestimation caused by the Vaisala RS80 pressure bias and its impact on meteorological profiles. *Atmospheric Measurement Techniques*, *8*(10), 4043–4054. https://doi.org/10.5194/amt-8-4043-2015
IPCC. (2014). Impacts of 1.5°C global warming on natural and human systems (Tech. Rep.). In *The intergovernmental panel on climate change*.
Isioye, O. A., Combrinck, L., Botai, J. O., & Munghemezulu, C. (2015). The potential for observing African weather with GNSS remote sensing. *Advances in Meteorology*, *2015*, 1–16. https://doi.org/10.1155/2015/723071
Joly, M., & Voldoire, A. (2009). Influence of ENSO on the west African monsoon: Temporal aspects and atmospheric processes. *Journal of Climate*, *22*(12), 3193–3210. https://doi.org/10.1175/2008jcli2450.1
Kalnay, E., Kanamitsu, M., Kistler, R., Collins, W., Deaven, D., Gandin, L., et al. (1996). The NCEP/NCAR 40-year reanalysis project [Dataset]. Soci, *77*(3), 437–472. https://doi.org/10.1175/1520-0477(1996)077<0437:TNYR>P2.0.CO;2
Kawatani, Y., Hamilton, K., Sato, K., Dunkerton, T. J., Watanabe, S., & Kikuchi, K. (2019). ENSO modulation of the QBO: Results from MIROC models with and without nonorographic gravity wave parameterization. *Journal of the Atmospheric Sciences*, *76*(12), 3893–3917. https://doi.org/10.1175/JAS-D-19-0163.1
Khandu, A. J., Wickert, J., Schmidt, T., Sharifi, M., Heck, B., & Fleming, K. (2011). GNSS remote sensing of the Australian tropopause. *Climatic Change*, *105*(3–4), 597–618. https://doi.org/10.1007/s10584-010-9894-6
Khandu, Awange, J., & Forootan, E. (2016). Interannual variability of upper tropospheric and lower stratospheric (UTLS) region over Ganges-Brahmaputra-Meghna basin based on COSMIC GNSS-RO data. *Atmospheric Measurement Techniques*, *8*(9), 9399–9453. https://doi.org/10.5194/amtd-8-9399-2015
Kubokawa, H., Satoh, M., Suzuki, J., & Fujiwara, M. (2016). Influence of topography on temperature variations in the tropical tropopause layer. *Journal of Geophysical Research: Atmospheres*, *121*(19), 11–556. https://doi.org/10.1002/2016JD025569
Kuo, Y.-H., Schreiner, W., Wang, J., Rossiter, D., & Zhang, Y. (2005). Comparison of GPS radio occultation soundings with radiosondes. *Geophysical Research Letters*, *32*(5), L05817. https://doi.org/10.1029/2004GL021443

Kursinski, E., Hajj, G., Schofield, J., Linfield, R., & Hardy, K. R. (1997). Observing Earth's atmosphere with radio occultation measurements using the Global Positioning System. *Journal of Geophysical Research*, *102*(D19), 23429–23465. https://doi.org/10.1029/97JD01569

L'Heureux, M. L., & Thompson, D. W. (2006). Observed relationships between the El Niño-Southern Oscillation and the extratropical zonal-mean circulation. *Journal of Climate*, *19*(2), 276–287. https://doi.org/10.1175/JCLI3617.1

Lamarque, J.-F., Langford, A., & Proffitt, M. (1996). Cross-tropopause mixing of ozone through gravity wave breaking: Observation and modeling. *Journal of Geophysical Research*, *101*(D17), 22969–22976. https://doi.org/10.1029/96JD02442

Lanzante, J. R., Klein, S. A., & Seidel, D. J. (2003). Temporal homogenization of monthly radiosonde temperature data. Part I: Methodology. *Journal of Climate*, *16*(2), 224–240. https://doi.org/10.1175/1520-0442(2003)016<0224:THOMRT>2.0.CO;2

Lavender, S. L., & Matthews, A. J. (2009). Response of the West African monsoon to the Madden–Julian oscillation. *Journal of Climate*, *22*(15), 4097–4116. https://doi.org/10.1175/2009JCLI2773.1

Lee, R. W., Woolnough, S. J., Charlton-Perez, A. J., & Vitart, F. (2019). ENSO modulation of MJO teleconnections to the North Atlantic and Europe. *Geophysical Research Letters*, *46*(22), 13535–13545. https://doi.org/10.1029/2019GL084683

Lien, G.-Y., Lin, C.-H., Huang, Z.-M., Teng, W.-H., Chen, J.-H., Lin, C.-C., et al. (2021). Assimilation impact of early FORMOSAT-7/COSMIC-2 GNSS radio occultation data with Taiwan's CWB global forecast system. *Monthly Weather Review*, *149*(7), 2171–2191. https://doi.org/10.1175/MWR-D-20-0267.1

Lim, E.-P., & Hendon, H. H. (2017). Causes and predictability of the negative Indian Ocean dipole and its impact on La Niña during 2016. *Scientific Reports*, *7*(1), 1–11. https://doi.org/10.1038/s41598-017-12674-z

Lin, H., Brunet, G., & Derome, J. (2009). An observed connection between the North Atlantic Oscillation and the Madden–Julian oscillation. *Journal of Climate*, *22*(2), 364–380. https://doi.org/10.1175/2008JCLI2515.1

Lu, J., Xie, F., Sun, C., Luo, J., Cai, Q., Zhang, J., et al. (2020). Analysis of factors influencing tropical lower stratospheric water vapor during 1980–2017. *npj Climate and Atmospheric Science*, *3*(1), 1–11. https://doi.org/10.1038/s41612-020-00138-7

Marshall, G. J. (2003). Trends in the southern annular mode from observations and reanalyses. *Journal of Climate*, *16*(24), 4134–4143. https://doi.org/10.1175/1520-0442(2003)016<4134:TITSAM>2.0.CO;2

McFarlane, N. (1987). The effect of orographically excited gravity wave drag on the general circulation of the lower stratosphere and troposphere. *Journal of the Atmospheric Sciences*, *44*(14), 1775–1800. https://doi.org/10.1175/1520-0469(1987)044<1775:TEOOEG>2.0.CO;2

McHugh, M. J., & Rogers, J. C. (2001). North Atlantic Oscillation influence on precipitation variability around the southeast African convergence zone. *Journal of Climate*, *14*(17), 3631–3642. https://doi.org/10.1175/1520-0442(2001)014<3631:NAOIOP>2.0.CO;2

Meng, L., Liu, J., Tarasick, D. W., & Li, Y. (2021). Biases of global tropopause altitude products in reanalyses and implications for estimates of tropospheric column ozone. *Atmosphere*, *12*(4), 417. https://doi.org/10.3390/atmos12040417

Moon, J.-Y., Wang, B., & Ha, K.-J. (2011). ENSO regulation of MJO teleconnection. *Climate Dynamics*, *37*(5–6), 1133–1149. https://doi.org/10.1007/s00382-010-0902-3

Nascimento, A., Awange, J., Gonçalves, R., & Khandu (2020). South America's tropopause variability in relation to global teleconnection (2001–2017): A GNSS-radio occultation assessment. *Journal of Atmospheric and Solar-Terrestrial Physics*, *209*, 105379. https://doi.org/10.1016/j.jastp.2020.105379

Neelin, J., Chou, C., & Su, H. (2003). Tropical drought regions in global warming and El Niño teleconnections. *Geophysical Research Letters*, *30*(24), 2275. https://doi.org/10.1029/2003GL018625

Nicholson, S. E. (2011). *Dryland climatology*. Cambridge University Press.

Nicholson, S. E., Barcilon, A., Challa, M., & Baum, J. (2007). Wave activity on the tropical easterly jet. *Journal of the Atmospheric Sciences*, *64*(7), 2756–2763. https://doi.org/10.1175/JAS3946.1

Nicholson, S. E., & Kim, J. (1997). The relationship of the El Niño-Southern Oscillation to African rainfall. *International Journal of Climatology*, *17*(2), 117–135. https://doi.org/10.1002/(SICI)1097-0088(199702)17:2<117::AID-JOC84>3.0.CO;2-O

Nicholson, S. E., & Klotter, D. (2021). The Tropical Easterly Jet over Africa, its representation in six reanalysis products, and its association with Sahel rainfall. *International Journal of Climatology*, *41*(1), 328–347. https://doi.org/10.1002/joc.6623

Noersomadi, Tsuda, T., & Fujiwara, M. (2019). Influence of ENSO and MJO on the zonal structure of tropical tropopause inversion layer using high-resolution temperature profiles retrieved from COSMIC GPS radio occultation. *Atmospheric Chemistry and Physics*, *19*(10), 6985–7000. https://doi.org/10.5194/acp-19-6985-2019

Pan, L. L., Honomichl, S. B., Bui, T. V., Thornberry, T., Rollins, A., Hintsa, E., & Jensen, E. J. (2018). Lapse rate or cold point: The tropical tropopause identified by in situ trace gas measurements. *Geophysical Research Letters*, *45*(19), 10–756. https://doi.org/10.1029/2018GL079573

Pan, L. L., Honomichl, S. B., Kinnison, D. E., Abalos, M., Randel, W. J., Bergman, J. W., & Bian, J. (2016). Transport of chemical tracers from the boundary layer to stratosphere associated with the dynamics of the Asian summer monsoon. *Journal of Geophysical Research: Atmospheres*, *121*(23), 14–159. https://doi.org/10.1002/2016jd025616

Parker, D. J., Fink, A., Janicot, S., Ngamini, J.-B., Douglas, M., Afiesimama, E., et al. (2008). The AMMA radiosonde program and its implications for the future of atmospheric monitoring over Africa. *Bulletin of the American Meteorological Society*, *89*(7), 1015–1028. https://doi.org/10.1175/2008BAMS2436.1

Pausata, F. S., Zanchettin, D., Karamperidou, C., Caballero, R., & Battisti, D. S. (2020). ITCZ shift and extratropical teleconnections drive ENSO response to volcanic eruptions. *Science Advances*, *6*(23). eaaz5006. https://doi.org/10.1126/sciadv.aaz5006

Peuch, V.-H. (2020). What are the atmospheric observation data gaps and what should WMO do to close them? In *WMO data conference: Exchange of Earth system data in the 21st century* (pp. 16–11). ECMWF.

Preisendorfer, R. W., & Mobley, C. D. (1988). Principal component analysis in meteorology and oceanography. *Bulletin of the American Meteorological Society*, *17*. 425.

Ramella-Pralungo, L., Haimberger, L., Stickler, A., & Brönnimann, S. (2014). A global radiosonde and tracked balloon archive on 16 pressure levels (GRASP) back to 1905–Part 1: Merging and interpolation to 00: 00 and 12: 00 GMT. *Earth System Science Data*, *6*(1), 185–200. https://doi.org/10.5194/essd-6-185-2014

Randel, W. J., & Park, M. (2006). Deep convective influence on the Asian summer monsoon anticyclone and associated tracer variability observed with Atmospheric Infrared Sounder (AIRS). *Journal of Geophysical Research*, *111*(D12), D12314. https://doi.org/10.1029/2005JD006490

Randel, W. J., Wu, F., & Gaffen, D. J. (2000). Interannual variability of the tropical tropopause derived from radiosonde data and NCEP reanalyses. *Journal of Geophysical Research*, *105*(D12), 15509–15523. https://doi.org/10.1029/2000JD900155

Rieckh, T., Scherllin-Pirscher, B., Ladstädter, F., & Foelsche, U. (2014). Characteristics of tropopause parameters as observed with GPS radio occultation. *Atmospheric Measurement Techniques*, *7*(11), 3947–3958. https://doi.org/10.5194/amt-7-3947-2014

Saji, N., Goswami, B., Vinayachandran, P., & Yamagata, T. (1999). A dipole mode in the tropical Indian Ocean. *Nature*, *401*(6751), 360–363. https://doi.org/10.1038/43854

Santer, B. D., Sausen, R., Wigley, T., Boyle, J., AchutaRao, K., Doutriaux, C., & Taylor, K. (2003). Behavior of tropopause height and atmospheric temperature in models, reanalyses, and observations: Decadal changes. *Journal of Geophysical Research*, *108*(D1), 4002. ACL–1. https://doi.org/10.1029/2002JD002258

Santer, B. D., Wehner, M. F., Wigley, T., Sausen, R., Meehl, G., Taylor, K., et al. (2003). Contributions of anthropogenic and natural forcing to recent tropopause height changes. *Science*, *301*(5632), 479–483. https://doi.org/10.1126/science.1084123

Scherllin-Pirscher, B., Foelsche, U., Lackner, B., & Kirchengast, G. (2007). Local time influence in single-satellite radio occultation climatologies from Sun-synchronous and non-Sun-synchronous satellites. *Journal of Geophysical Research*, *112*(D11), D11119. https://doi.org/10.1029/2006JD007934

Scherllin-Pirscher, B., Deser, C., Ho, S.-P., Chou, C., Randel, W., & Kuo, Y.-H. (2012). The vertical and spatial structure of ENSO in the upper troposphere and lower stratosphere from GPS radio occultation measurements. *Geophysical Research Letters*, *39*(20), L20801. https://doi.org/10.1029/2012GL053071

Scherllin-Pirscher, B., Kirchengast, G., Steiner, A. K., Kuo, Y.-H., & Foelsche, U. (2011). Quantifying uncertainty in climatological fields from GPS radio occultation: An empirical-analytical error model. *Atmospheric Measurement Techniques*, *4*(9), 2019–2034. https://doi.org/10.5194/amt-4-2019-2011

Scherllin-Pirscher, B., Steiner, A., Kirchengast, G., Kuo, Y.-H., & Foelsche, U. (2011). Empirical analysis and modeling of errors of atmospheric profiles from GPS radio occultation. *Atmospheric Measurement Techniques*, *4*(9), 1875–1890. https://doi.org/10.5194/amt-4-1875-2011

Scherllin-Pirscher, B., Steiner, A. K., Anthes, R. A., Alexander, M. J., Alexander, S. P., Biondi, R., et al. (2021). Tropical temperature variability in the UTLS: New insights from GPS radio occultation observations. *Journal of Climate*, *34*(8), 2813–2838. https://doi.org/10.1175/JCLI-D-20-0385.1

Scherllin-Pirscher, B., Steiner, A. K., Kirchengast, G., Schwärz, M., & Leroy, S. S. (2017). The power of vertical geolocation of atmospheric profiles from GNSS radio occultation. *Journal of Geophysical Research: Atmospheres*, *122*(3), 1595–1616. https://doi.org/10.1002/2016JD025902

Schott, F. A., Xie, S.-P., & McCreary, J. P., Jr. (2009). Indian Ocean circulation and climate variability. *Reviews of Geophysics*, *47*(1), RG1002. https://doi.org/10.1029/2007RG000245

Schreiner, W., Rocken, C., Sokolovskiy, S., Syndergaard, S., & Hunt, D. (2007). Estimates of the precision of GPS radio occultations from the COSMIC/FORMOSAT-3 mission. *Geophysical Research Letters*, *34*(4), L04808. https://doi.org/10.1029/2006gl027557

Schreiner, W., Weiss, J., Anthes, R., Braun, J., Chu, V., Fong, J., et al. (2020). COSMIC-2 radio occultation constellation: First results. *Geophysical Research Letters*, *47*(4), e2019GL086841. https://doi.org/10.1029/2019GL086841

Seidel, D. J., Angell, J., Christy, J., Free, M., Klein, S., Lanzante, J. R., et al. (2004). Uncertainty in signals of large-scale climate variations in radiosonde and satellite upper-air temperature datasets. *Journal of Climate*, *17*(11), 2225–2240. https://doi.org/10.1175/1520-0442(2004)017<2225:UISOLC>2.0.CO;2

Shangguan, M., Wang, W., & Jin, S. (2019). Variability of temperature and ozone in the upper troposphere and lower stratosphere from multi-satellite observations and reanalysis data. *Atmospheric Chemistry and Physics*, *19*(10), 6659–6679. https://doi.org/10.5194/acp-19-6659-2019

Silvestri, G., & Vera, C. (2009). Nonstationary impacts of the southern annular mode on Southern Hemisphere climate. *Journal of Climate*, *22*(22), 6142–6148. https://doi.org/10.1175/2009JCLI3036.1

Simmons, A., Soci, C., Nicolas, J., Bell, B., Berrisford, P., Dragani, R., et al. (2020). *Global stratospheric temperature bias and other stratospheric aspects of ERA5 and ERA5. 1*. ECMWF. https://doi.org/10.21957/rcxqfmg0

Staten, P. W., & Reichler, T. (2008). Use of radio occultation for long-term tropopause studies: Uncertainties, biases, and instabilities. *Journal of Geophysical Research*, *113*(D7), D00B05. https://doi.org/10.1029/2008JD009886

Steinbrecht, W., Claude, H., Köhler, U., & Hoinka, K. (1998). Correlations between tropopause height and total ozone: Implications for long-term changes. *Journal of Geophysical Research*, *103*(D15), 19183–19192. https://doi.org/10.1029/98JD01929

Steinbrecht, W., Claude, H., Schönenborn, F., Leiterer, U., Dier, H., & Lanzinger, E. (2008). Pressure and temperature differences between Vaisala RS80 and RS92 radiosonde systems. *Journal of Atmospheric and Oceanic Technology*, *25*(6), 909–927. https://doi.org/10.1175/2007JTECHA999.1

Steiner, A., Lackner, B., Ladstädter, F., Scherllin-Pirscher, B., Foelsche, U., & Kirchengast, G. (2011). GPS radio occultation for climate monitoring and change detection. *Radio Science*, *46*(06), 1–17. https://doi.org/10.1029/2010RS004614

Sultan, B., & Janicot, S. (2003). The West African monsoon dynamics. Part II: The "preonset" and "onset" of the summer monsoon. *Journal of Climate*, *16*(21), 3407–3427. https://doi.org/10.1175/1520-0442(2003)016<3407:TWAMDP>2.0.CO;2

Taalas, P., Steiner, A., & Andersen, I. (2021). COP26: How plugging data gaps will transform our response to climate change [Conference]. Retrieved from https://www.scmp.com/https://www.scmp.com/%20(visited:%202021-12-10)

Taguchi, M. (2010). Observed connection of the stratospheric quasi-biennial oscillation with El Niño-Southern Oscillation in radiosonde data. *Journal of Geophysical Research*, *115*(D18), D18120. https://doi.org/10.1029/2010JD014325

Tegtmeier, S., Anstey, J., Davis, S., Dragani, R., Harada, Y., Ivanciu, I., et al. (2020). Temperature and tropopause characteristics from reanalyses data in the tropical tropopause layer. *Atmospheric Chemistry and Physics*, *20*(2), 753–770. https://doi.org/10.5194/acp-20-753-2020

Terink, W., Immerzeel, W. W., & Droogers, P. (2013). Climate change projections of precipitation and reference evapotranspiration for the Middle East and Northern Africa until 2050. *International Journal of Climatology*, *33*(14), 3055–3072. https://doi.org/10.1002/joc.3650

Thompson, A. M., Balashov, N. V., Witte, J., Coetzee, J., Thouret, V., & Posny, F. (2014). Tropospheric ozone increases over the southern Africa region: Bellwether for rapid growth in southern hemisphere pollution? *Atmospheric Chemistry and Physics*, *14*(18), 9855–9869. https://doi.org/10.5194/acp-14-9855-2014

Thomson, M. C., Connor, S. J., Zebiak, S. E., Jancloes, M., & Mihretie, A. (2011). Africa needs climate data to fight disease. *Nature*, *471*(7339), 440–442. https://doi.org/10.1038/471440a

Thorne, P., & Vose, R. (2010). Reanalyses suitable for characterizing long-term trends. *Bulletin of the American Meteorological Society*, *91*(3), 353–362. https://doi.org/10.1175/2009BAMS2858.1

Towner, J., Cloke, H. L., Zsoter, E., Flamig, Z., Hoch, J. M., Bazo, J., et al. (2019). Assessing the performance of global hydrological models for capturing peak river flows in the Amazon basin. *Hydrology and Earth System Sciences*, *23*(7), 3057–3080. https://doi.org/10.5194/hess-23-3057-2019

Trenberth, K. E., & Stepaniak, D. P. (2001). Indices of El Niño evolution. *Journal of Climate*, *14*(8), 1697–1701. https://doi.org/10.1175/1520-0442(2001)014<1697:LIOENO>2.0.CO;2

UCAR COSMIC Program. (2006). COSMIC data products [Dataset]. UCAR/NCAR - COSMIC. Retrieved from https://doi.org/10.5065/ZD80-KD74

UCAR COSMIC Program. (2019). COSMIC-2 data products [Dataset]. UCAR/NCAR - COSMIC. Retrieved from https://doi.org/10.5065/t353-c093

Ummenhofer, C. C., & England, M. H. (2007). Interannual extremes in New Zealand precipitation linked to modes of southern hemisphere climate variability. *Journal of Climate*, *20*(21), 5418–5440. https://doi.org/10.1175/2007JCLI1430.1

van der Linden, R., Knippertz, P., Fink, A. H., Ingleby, B., Maranan, M., & Benedetti, A. (2020). The influence of DACCIWA radiosonde data on the quality of ECMWF analyses and forecasts over southern West Africa. *Quarterly Journal of the Royal Meteorological Society*, *146*(729), 1719–1739. https://doi.org/10.1002/qj.3763

Virts, K. S., & Wallace, J. M. (2014). Observations of temperature, wind, cirrus, and trace gases in the tropical tropopause transition layer during the MJO. *Journal of the Atmospheric Sciences*, *71*(3), 1143–1157. https://doi.org/10.1175/JAS-D-13-0178.1

Wang, J., & Zhang, L. (2008). Systematic errors in global radiosonde precipitable water data from comparisons with ground-based GPS measurements. *Journal of Climate*, *21*(10), 2218–2238. https://doi.org/10.1175/2007JCLI1944.1

Wang, W., Matthes, K., Omrani, N.-E., & Latif, M. (2016). Decadal variability of tropical tropopause temperature and its relationship to the Pacific Decadal Oscillation. *Scientific Reports*, *6*(1), 1–12. https://doi.org/10.1038/srep29537

Westra, S., Brown, C., Lall, U., Koch, I., & Sharma, A. (2010). Interpreting variability in global SST data using independent component analysis and principal component analysis. *International Journal of Climatology*, *30*(3), 333–346. https://doi.org/10.1002/joc.1888

Wheeler, M. C., & Hendon, H. H. (2004). An all-season real-time multivariate MJO index: Development of an index for monitoring and prediction. *Monthly Weather Review*, *132*(8), 1917–1932. https://doi.org/10.1175/1520-0493(2004)132<1917:AARMMI>2.0.CO;2

Wickert, J. (2004). *Comparison of vertical refractivity and temperature profiles from CHAMP with radiosonde measurements (Tech. Rep.)*. GFZ German Research Centre for Geosciences.

Wickert, J., Beyerle, G., König, R., Heise, S., Grunwaldt, L., Michalak, G., et al. (2005). GPS radio occultation with CHAMP and GRACE: A first look at a new and promising satellite configuration for global atmospheric sounding. *Annales Geophysicae*, *23*(3), 653–658. https://doi.org/10.5194/angeo-23-653-2005

WMO. (1957). Meteorology-A three-dimensional science: Second session of the commission for aerology. *World Meteorological Organization Bulletin*, *4*(4), 134–138.

WMO. (2020). *The gaps in the global basic observing network (GBON) (Tech. Rep.)*. World Meteorological Organization.

World Meteorological Organization. (2020). WMO codes registry [Collection]. Retrieved from http://codes.wmo.int/.%20WMO

Xian, T., & Homeyer, C. R. (2019). Global tropopause altitudes in radiosondes and reanalyses. *Atmospheric Chemistry and Physics*, *19*, 5661–5678. https://doi.org/10.5194/acp-2018-945

Zeng, Z., Ho, S.-P., Sokolovskiy, S., & Kuo, Y.-H. (2012). Structural evolution of the Madden-Julian Oscillation from COSMIC radio occultation data. *Journal of Geophysical Research*, *117*(D22), D22108. https://doi.org/10.1029/2012JD017685